nature medicine

ARTICLES

https://doi.org/10.1038/s41591-018-0102-y

Cold-induced epigenetic programming of the sperm enhances brown adipose tissue activity in the offspring

Wenfei Sun[1,9], Hua Dong[1,9], Anton S. Becker[1,2,3], Dianne H. Dapito[1], Salvatore Modica[1], Gerald Grandl[1], Lennart Opitz[1,4], Vissarion Efthymiou[1], Leon G. Straub[1], Gitalee Sarker[1], Miroslav Balaz[1], Lucia Balazova[1], Aliki Perdikari[1], Elke Kiehlmann[1], Sara Bacanovic[3], Caroline Zellweger[3], Daria Peleg-Raibstein[1], Pawel Pelczar[5], Wolf Reik[6,7], Irene A. Burger[3], Ferdinand von Meyenn[6,8] and Christian Wolfrum[1]*

Recent research has focused on environmental effects that control tissue functionality and systemic metabolism. However, whether such stimuli affect human thermogenesis and body mass index (BMI) has not been explored. Here we show retrospectively that the presence of brown adipose tissue (BAT) and the season of conception are linked to BMI in humans. In mice, we demonstrate that cold exposure (CE) of males, but not females, before mating results in improved systemic metabolism and protection from diet-induced obesity of the male offspring. Integrated analyses of the DNA methylome and RNA sequencing of the sperm from male mice revealed several clusters of co-regulated differentially methylated regions (DMRs) and differentially expressed genes (DEGs), suggesting that the improved metabolic health of the offspring was due to enhanced BAT formation and increased neurogenesis. The conclusions are supported by cell-autonomous studies in the offspring that demonstrate an enhanced capacity to form mature active brown adipocytes, improved neuronal density and more norepinephrine release in BAT in response to cold stimulation. Taken together, our results indicate that in humans and in mice, seasonal or experimental CE induces an epigenetic programming of the sperm such that the offspring harbor hyperactive BAT and an improved adaptation to overnutrition and hypothermia.

In 2016, 39% of all adults worldwide were classified as being overweight (BMI > 25) and 13% as being clinically obese (BMI > 30)[1]. This imposes a burden on society because obesity-associated comorbidities, which are linked to an increase in adipose tissue mass, are the main contributors to overall mortality and healthcare costs. Adipose tissue functions as a dynamic endocrine organ[2], and, therefore, its 'quality' is considered to be an important factor in the development of obesity-associated comorbidities[3]. Adipose tissue can be divided into the functionally and morphologically distinct white adipose tissue (WAT) and BAT[4]. The main function of BAT is energy dissipation via nonshivering thermogenesis[5], which is enabled by the presence of uncoupling protein 1 (UCP1) in the inner mitochondrial membrane. Thus, brown adipocytes contribute to the maintenance of body temperature during acute and chronic CE[2,6].

Besides the classical BAT found in rodents in the interscapular area (iBAT), a second type of thermogenic active fat cell (termed beige or brite adipocytes) has been described, which is induced by CE mainly in inguinal WAT (ingWAT)[7]. Analysis of [^{18}F]fluorodeoxyglucose (FDG)-PET and FDG–CT scans (hereafter collectively referred to as FDG-PET/CT scans) have demonstrated the presence of active BAT in adult humans in the supraclavicular, paravertebral and deep neck regions[8–13], and human BAT can be activated by mild CE or by administration of a specific β3-adrenergic receptor (ADRB3) agonist[14,15]. The relevance of BAT for physiology was inferred by the association with various metabolic parameters[15], and it was demonstrated that people with functional BAT can effectively lose weight by a mild cold-stimulation regime[16].

In recent years, studies have demonstrated a link between paternal preconception nutrient exposure and the phenotype of the offspring[17,18]. Differences in gene expression patterns arise during development and can be retained through mitosis by epigenetic mechanisms[19]. In the context of thermoregulation, it has been shown that environmentally induced changes in gene expression can affect cellular function and thereby also the predisposition to certain diseases[20]. Additionally, changes in the environment can be transmitted to subsequent generations[18,21,22]. More specifically, there have been indications that the season of birth and adult BMI show some correlation[23]. Here we studied the influence of environmental temperature and its effect on systemic metabolism, as well as the contribution of different thermogenic pathways, using human and mouse studies.

Results

Cold exposure before conception and during gestation activates brown and brite adipose tissue. To identify a possible correlation

[1]Institute of Food, Nutrition and Health, ETH Zurich, Schwerzenbach, Switzerland. [2]Institute of Diagnostic and Interventional Radiology, University Hospital of Zurich, Zurich, Switzerland. [3]Clinic of Nuclear Medicine, University Hospital of Zurich, Zurich, Switzerland. [4]Functional Genomics Center Zurich, ETH Zurich–University of Zurich, Zurich, Switzerland. [5]Center for Transgenic Models, University of Basel, Basel, Switzerland. [6]Epigenetics Program, Babraham Institute, Cambridge, UK. [7]Wellcome Trust Sanger Institute, Hinxton, UK. [8]Department of Medical and Molecular Genetics, King's College London, London, UK. [9]These authors contributed equally: Wenfei Sun and Hua Dong. *e-mail: christian-wolfrum@ethz.ch

between ambient temperature and BAT abundance, we performed a retrospective study of FDG-PET/CT scans from 2007–2015 that were collected from the University Hospital of Zurich ($n=8,440$ individuals). Representative PET images from two individuals are shown in Supplementary Fig. 1a. Individuals with active BAT were 3.2% more likely to have been conceived in the colder period of the year, for example, between October and February (mean temperature estimate 2 °C), whereas individuals without active BAT were more likely to have been conceived in the warmer months, for example, between April and September (mean temperature estimate 13 °C) (Fig. 1a). No apparent fluctuations in age (Supplementary Fig. 1b) or BMI (Supplementary Fig. 1c) were observed, and the pattern persisted for different BAT activation strengths (Supplementary Fig. 1d). Among individuals who were conceived in the colder period ($n=3,793$), BAT-positive individuals ($n=235$) had a significantly lower BMI (mean 20.9 versus 22.8; $P<0.001$) than age- and sex-matched BAT-negative individuals (Fig. 1b). These data identified a correlation between the season of conception and the propensity to form active BAT; however, given the retrospective nature and the large number of potential confounders, causality could not be inferred. Hence, we investigated the effect of CE before and during conception using mouse model systems. We analyzed offspring groups whose parents had not been exposed to cold (23 °C) (group 1) or had been exposed to cold (8 °C) either before conception (group 2), before conception and during the first week of gestation (group 3) or before conception and during weeks 1 and 2 of gestation (group 4) (Fig. 1c). Notably, we observed that offspring from parents that were exposed to cold before conception showed higher UCP1 expression in both iBAT and ingWAT under regular housing conditions (RT) (Fig. 1d). When we challenged offspring by CE, the effect on UCP1 expression was markedly enhanced (Fig. 1e and Supplementary Fig. 1e). Taken together, our data indicated that CE of parents before conception or during gestation resulted in higher basal and stimulated UCP1 expression in the iBAT and ingWAT of the offspring.

The effects of preconception cold exposure are mediated through the paternal lineage. On the basis of these findings, we analyzed whether the observed effect of CE was transmitted through the paternal (P-CE) or maternal (M-CE) lineage by focusing on the preconception exposure model in all subsequent studies. Notably, we observed that the effects of parental CE on UCP1 expression at RT were mediated by the paternal lineage (Fig. 2a) and that the effect was enhanced in the iBAT and ingWAT of male offspring and in the iBAT of female offspring after stimulation by CE (Fig. 2b and Supplementary Fig. 2a). Also, we could show that offspring from P-CE mice (hereafter referred to as P-CE offspring) had higher UCP1 protein levels than those from control (Ctrl) males at 21 d of age at RT and under thermoneutral (TN) conditions (Supplementary Fig. 2b,c). Analysis of gene expression in the iBAT of P-CE offspring demonstrated higher mRNA expression of several markers of brown-fat function in iBAT (Fig. 2c). We did not observe any changes in litter size and in nursing percentages over the postnatal period (Supplementary Fig. 2d,e), suggesting that alterations in maternal behavior were not the cause for the observed phenotype. To exclude paternal behavior as a confounding factor, we performed in vitro fertilization (IVF) with sperm derived from P-CE or Ctrl males. We observed an induction of brown fat marker expression (Supplementary Fig. 2f) and UCP1 protein (Fig. 2d and Supplementary Fig. 2g) in the iBAT of both male and female offspring derived from P-CE versus Ctrl sperm, which was paralleled by a difference in body surface temperature (Supplementary Fig. 2h).

Because brown fat is formed at embryonic day 15.5 (E15.5)[24], we analyzed whether the observed changes were already present before birth. We could show that in iBAT from E18.5 embryos, *Ucp1* mRNA and other brown fat markers were higher in P-CE than Ctrl offspring (Supplementary Fig. 2i). Notably, these changes did not translate into an altered birth weight nor did we observe differences in postnatal weight gain (Supplementary Fig. 2j). However, iBAT weight in 7-week-old P-CE mice was significantly higher than Ctrl ($P=0.003$; Supplementary Fig. 2k), suggesting that not only expression of UCP1, but also the formation of iBAT, was enhanced in P-CE offspring. Consistent with this, we could show by immunohistochemical analysis of iBAT and ingWAT that the area of UCP1$^+$ patches, which denote cells with high levels of UCP1 expression, was higher at RT in both iBAT and ingWAT (Fig. 2e,f). After CE, this phenotype was enhanced in both iBAT and ingWAT (Fig. 2g,h). We also observed a lower lipid droplet size in the ingWAT of P-CE offspring, suggesting more active lipid metabolism (Supplementary Fig. 2l). Furthermore, reduced adipocyte size and greater numbers of UCP1$^+$ cells were observed in P-CE offspring at 21 d of age at RT or at TN (Supplementary Fig. 2m–o). Taken together, our data demonstrated that the effect of CE was mediated through the paternal lineage and affected both UCP1 expression and adipose tissue morphology.

Cold exposure of paternal mice induces iBAT activity and systemic metabolism in the offspring. On the basis of these findings, we analyzed whether the effect of P-CE would translate into a higher thermogenic activity. Surface temperature was higher in P-CE offspring than in Ctrl offspring at postnatal day (P) 7 (Fig. 3a) at RT. At 7 weeks of age, mice had the same body weight (Supplementary Fig. 3a) and the same surface temperature (Fig. 3b) at RT, whereas after CE, the P-CE offspring exhibited a higher surface temperature (Fig. 3b). Furthermore, we observed that P-CE offspring had an 11% higher volume of oxygen consumption rate (VO_2) and volume of carbon dioxide production rate (VCO_2) at RT, which was enhanced after acute CE (Fig. 3c and Supplementary Fig. 3b), whereas the respiratory exchange ratio (RER) remained unchanged (Supplementary Fig. 3c). Because CE can lead to shivering, we quantified the induction of brown fat in response to an intraperitoneal (i.p.) injection of ADRB3 agonist CL316,243 (CL). We observed higher amounts of UCP1 protein (Fig. 3d) and higher VO_2 and VCO_2 levels (Fig. 3e and Supplementary Fig. 3d), which was concomitant with more UCP1$^+$ cells in the iBAT (Fig. 3f) of P-CE mice. Of note, we could show a lower RER in P-CE offspring following CL injection, suggesting a preferred utilization of fatty acids (Supplementary Fig. 3e).

On the basis of these data, we analyzed whether the changes in respiration could lead to altered systemic metabolism. We did not observe any changes in body weight between 7 and 18 weeks of age (Supplementary Fig. 3f) when P-CE and Ctrl offspring were fed a regular chow diet at RT. Similarly, we did not observe any change in food intake (Supplementary Fig. 3g); however, we could show that P-CE offspring showed a substantial reduction in basal glucose levels, as well as a trend for improved insulin sensitivity (Supplementary Fig. 3h). Insulin, cholesterol and fibroblast growth factor 21 (FGF21) levels were the same in both groups of offspring (Supplementary Fig. 3i–k), and P-CE offspring showed lower circulating triacylglycerol (TAG) levels (Supplementary Fig. 3l) and higher circulating non-esterified fatty acid (NEFA) levels under fasted conditions (Fig. 3g). To assess whether the changes in altered glucose homeostasis could be due to a higher glucose uptake into iBAT, we injected Ctrl and P-CE offspring at RT or after CE with radiolabeled 2-deoxyglucose. We observed higher glucose uptake exclusively into iBAT and ingWAT of P-CE offspring, whereas glucose uptake in muscle, brain, liver and heart was not affected (Fig. 3h and Supplementary Fig. 3m). These changes were paralleled by an induction of facilitated glucose transporter member 4 (GLUT4) expression in iBAT under CE (Fig. 3i). Taken together, our data demonstrate that P-CE induces brown and brite adipocyte function in the offspring, which leads to an improved systemic metabolism.

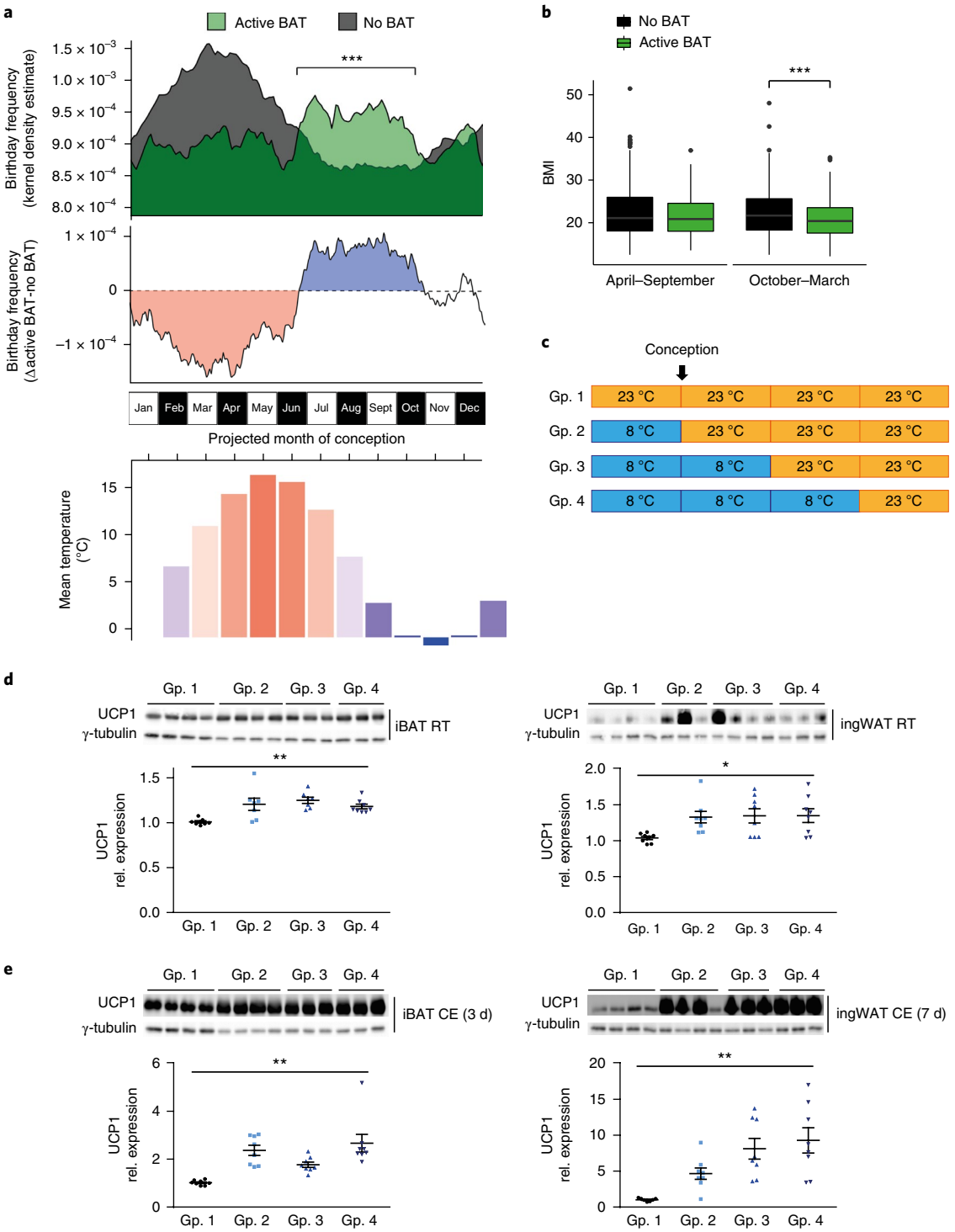

Fig. 1 | Parental cold exposure induces UCP1 expression in iBAT and ingWAT. a, The birth day frequency of individuals with no active BAT (no BAT) and active BAT (top) and the ratio of such individuals as a function of birth date (middle). BAT activity was measured by FDG-PET/CT scans ($n = 8{,}440$ individuals, $P = 1 \times 10^{-16}$). Bottom, monthly mean temperatures in Switzerland, to serve as a visual illustration of the warmer and colder periods. **b**, BMI of BAT-negative (black boxes) and BAT-positive (green boxes) individuals born between April and September and between October and March ($n = 914$ individuals). Vertical bars are estimated 95% confidence intervals (CIs); the middle line represents the median, the top and bottom line the 75th and 25th percentile, respectively, the whiskers have the length of 1.5 × the interquartile range. $P = 0.00091$ by two-sided t-test, Bonferroni-corrected. **c**, Scheme for the parental CE mouse model. 10-week-old male and female C57BL/6 mice were cold-stimulated for 0 (group 1; Gp. 1), 7 (group 2; Gp. 2), 14 (group 3; Gp. 3) or 21 d (group 4; Gp. 4) at 8 °C, then returned to 23 °C. Each block denotes 1 week; breeding was initiated at the end of the block 1. **d**,**e**, Cropped western blots of UCP1 (γ-tubulin is the loading control) in iBAT and ingWAT from the four experimental groups of offspring described in **c**; tissues were isolated while the mice were at RT (**d**) or after CE (**e**). Shown is one representative blot from four independent experiments; graphs depict mean of litter from all experiments ± s.e.m.; n = number of litters tested, each dot represents one litter. Results are mean ± s.e.m. (**d**, left: $n = 7$, $F_{(3,24)} = 6.48$; **d**, right: $n = 8$, $F_{(3,28)} = 3.52$; **e**, left: $n = 8$, $F_{(3,28)} = 10.90$; **e**, right, $n = 8$, $F_{(3,28)} = 8.65$). Statistical significance was calculated using one-way analysis of variance (ANOVA); $^{*}P < 0.05$, $^{**}P < 0.01$, $^{***}P < 0.001$.

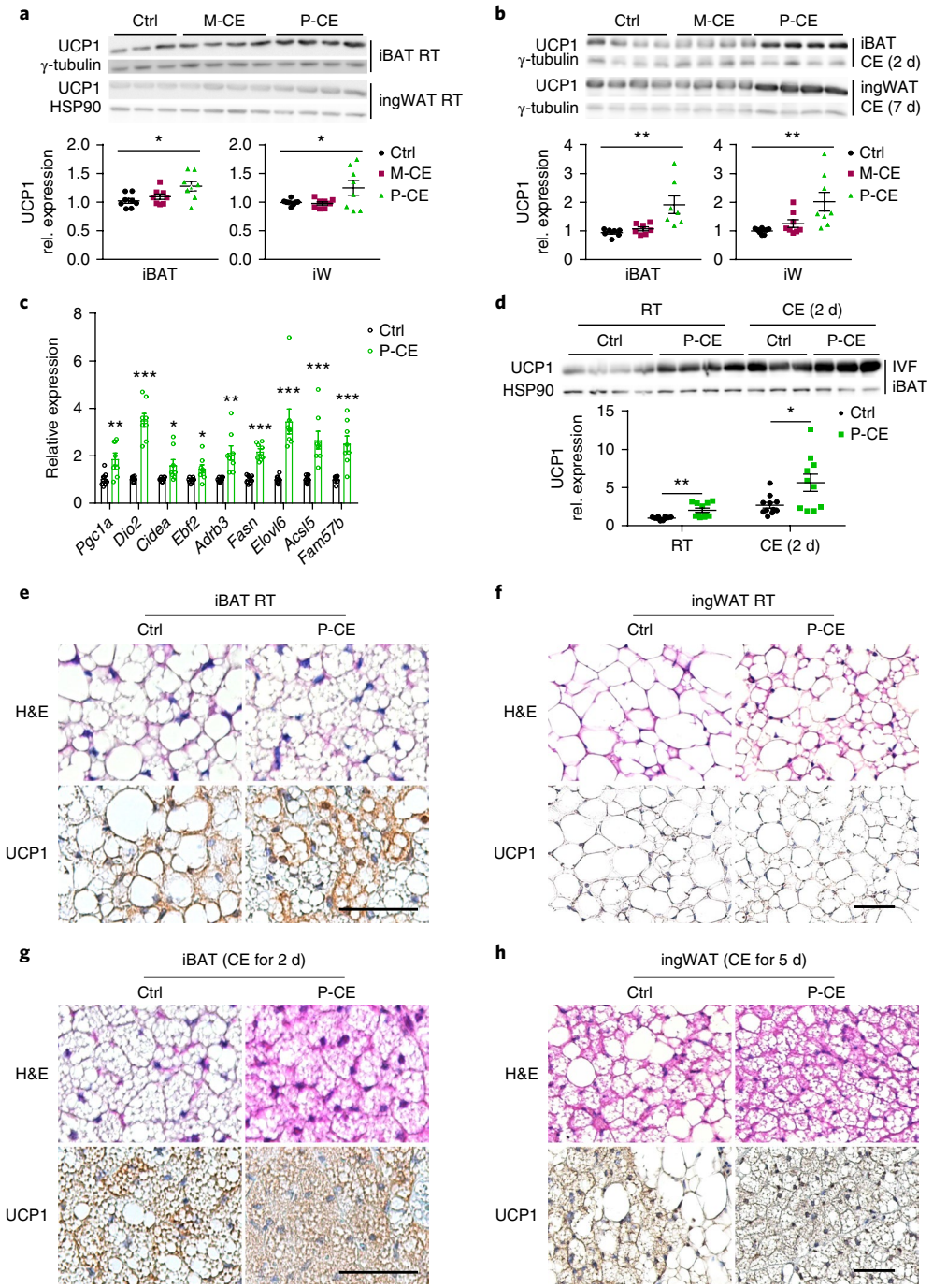

Fig. 2 | Paternal cold exposure exclusively induces UCP1 expression in iBAT and ingWAT. a,**b**, Either female (M-CE) or male (P-CE) mice were cold-stimulated for 7 d before initiating a mating. All mice were kept at 23 °C afterwards. Shown are cropped western blots of UCP1 (γ-tubulin and HSP90 were used as loading controls) from iBAT and ingWAT isolated from mice in the three experimental groups of offspring of Ctrl, M-CE and P-CE while the mice were at RT (**a**) or after CE (**b**). **c**, mRNA levels of different brown fat markers in the iBAT of Ctrl and P-CE offspring at RT ($n = 8$ litters per group). Expression was normalized by ΔC_t values. **d**, Cropped western blots of UCP1 in the iBAT (HSP90 was used as the loading control) from the IVF offspring of Ctrl and P-CE at RT and after 2 d of CE, ($n = 11$ litters for Ctrl; $n = 10$ litters for P-CE). **e–h**, Representative hematoxylin and eosin (H&E) and UCP1 immunohistochemistry staining of iBAT (**e**,**g**) and ingWAT (**f**,**h**) from Ctrl or P-CE offspring at 23 °C (**e**,**f**) and 8 °C (**g**,**h**). **e**,**f**: $n = 8$ litters per group, **g**,**h**: $n = 6$ litters per group. Scale bar, 100 µm. Throughout, data are mean ± s.e.m.; each dot represents one litter (n = litters per group; **a**, left: $n = 8$, $F_{(2,21)} = 4.93$, $P = 0.018$; **a**, right: $n = 8$, $F_{(2,21)} = 3.92$, $P = 0.036$; **b**, left: $n = 7$, $F_{(2,18)} = 8.27$, $P = 0.003$; **b**, right: $n = 8$, $F_{(2,21)} = 7.74$, $P = 0.003$; **d**, left: $P = 0.003$; **d**, right: $P = 0.02$). $^*P < 0.05$; $^{**}P < 0.01$; $^{***}P < 0.001$; by one-way ANOVA (**a**,**b**) or two-tailed unpaired Student's t-test (**c**,**d**).

The effect of cold-exposed paternal mice is mediated in part through brown and brite adipocytes. Because several tissues contribute to the maintenance of body temperature, we next aimed to assess the contribution of brown and brite adipocytes. Therefore, we used a transgenic mouse line that expressed a diphtheria toxin receptor (DTR) fused to green fluorescent protein (GFP) under the control of the *Ucp1* promoter (hereafter referred to as Ucp1-DTR-GFP mice)[25]. Sequential injections of diphtheria toxin A (DTA)

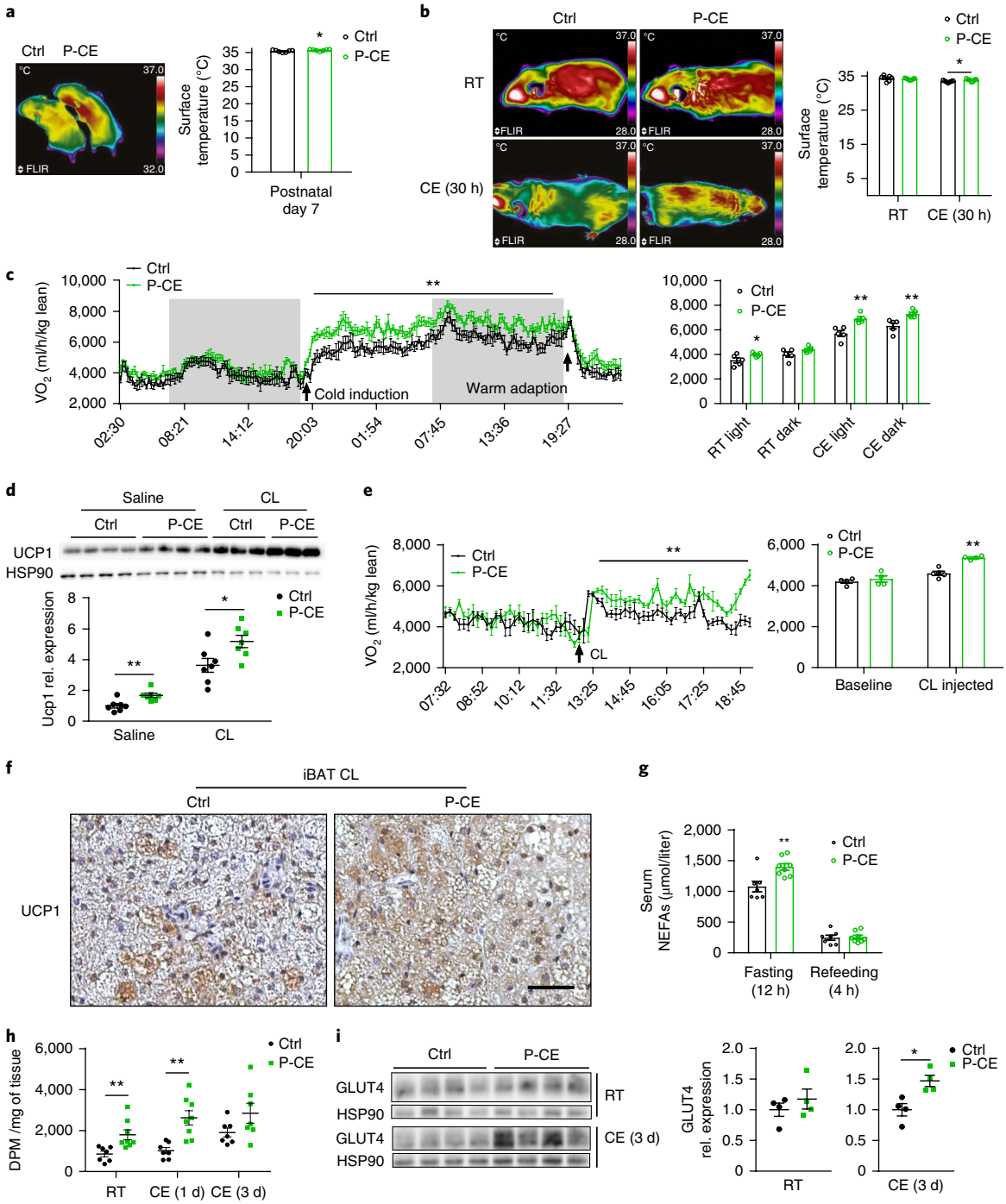

Fig. 3 | Paternal cold exposure induces oxygen consumption in offspring after cold or ADRB3 agonist stimulation. a, Left, representative thermographic image of Ctrl and P-CE offspring at postnatal day 7. Offspring were kept at RT. Right, calculated averages of surface temperature ($n = 7$ litters). $P = 0.04$. **b**, Representative thermographic image (left) and calculated averages of surface temperature (right) of Ctrl and P-CE offspring at 23 °C and after 30 h of CE ($n = 7$ litters). P (30-h CE) = 0.03. **c**, Time-resolved oxygen consumption in Ctrl and P-CE offspring mice, with cold induction (arrow) followed by warm adaption (arrow); dark phase is marked as dark background; right inset depicts calculated means as indicated ($n = 5$ litters). $P = 0.006$. **d**, Cropped western blots of UCP1 from iBAT (HSP90 was used as the loading control) of Ctrl and P-CE offspring that were injected with saline or CL (0.1 mg per kg body weight, three times, every 24 h, $n = 7$ litters). **e**, Time-resolved oxygen consumption of Ctrl ($n = 4$ litters) and P-CE ($n = 5$ litters) offspring, before and after (arrow) injection of CL (arrow). $P = 0.003$. **f**, Representative images of UCP1 staining of iBAT from Ctrl or P-CE offspring after injection with CL ($n = 6$ litters per group). Scale bar, 100 µm. **g**, Serum NEFAs level of fasted (12 h) and re-fed (4 h) mice from the Ctrl ($n = 7$ litters) and P-CE ($n = 8$ litters) groups. **h**, Glucose uptake in BAT at RT, after 1 d or 3 d of CE ($n = 7$ litters for all groups, except $n = 8$ for the P-CE at RT and 1 d CE groups). **i**, Western blots of GLUT4 in the iBAT (HSP90 was used as the loading control) isolated from Ctrl or P-CE offspring at RT and after 3 d of CE ($n = 4$ litters). Throughout, results are mean ± s.e.m.; each dot represents one litter. Statistical significance was calculated by a two-tailed unpaired Student's t-test; $^*P < 0.05$, $^{**}P < 0.01$.

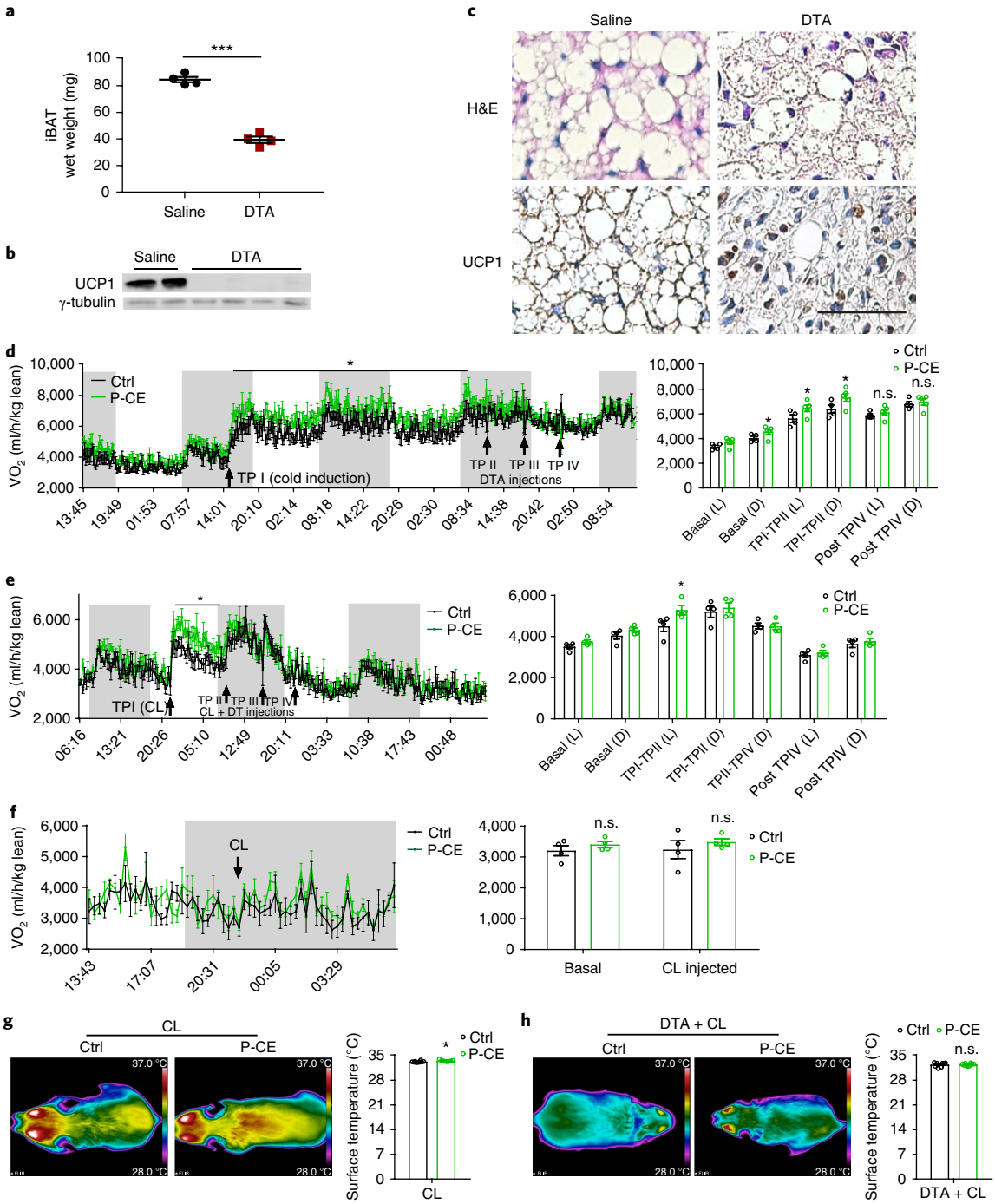

Fig. 4 | Paternal cold exposure induces oxygen consumption in offspring due to increased BAT functionality. a,**b**, Tissue wet weight ($n=4$ mice per group; $P=0.000001$) (**a**) and cropped western blots of UCP1 in the iBAT (γ-tubulin was used as the loading control) (**b**) from Ucp1-DTR-GFP mice (11-weeks of age) after treatment with saline or DTA. **c**, Representative H&E (top) and UCP1 (bottom) staining of iBAT from Ucp1-DTR-GFP mice after saline (left) or DTA (right) injection ($n=4$ mice per group). Scale bar, 100 µm. **d**, Time-resolved oxygen consumption in Ucp1-DTR-GFP Ctrl ($n=4$ litters) and P-CE ($n=5$ litters) offspring after cold induction (TP I) followed by three DTA injections (TP II–IV). Graph shows calculated means as indicated in the light cycle (L) and dark cycle (D); dark phase is marked as dark background. $P=0.04$. **e**, Time-resolved oxygen consumption in Ucp1-DTR-GFP Ctrl and P-CE offspring after CL injection (TP I) followed by three DTA + CL injections (TP II–IV). Graph depicts calculated mean as indicated ($n=4$ litters). $P=0.03$. **f**, Time-resolved oxygen consumption in Ucp1-DTR-GFP Ctrl and P-CE offspring 24 h after BAT depletion (TP IV in **e**) and stimulation with CL (arrow) ($n=4$ litters). **g**,**h**, Representative thermographic images of Ctrl and P-CE offspring that were subjected to CL stimulation before (**g**) or after (**h**) BAT depletion. Graphs depict calculated averages ($n=8$ litters). Throughout, results are mean ± s.e.m. Statistical significance was calculated by a two-tailed unpaired Student's *t*-test; $^*P<0.05$, $^{***}P<0.001$; n.s., not significant.

in these mice led to the complete ablation of brown adipocytes, as indicated by the reduction in iBAT mass (Fig. 4a) and loss of UCP1 protein expression in the iBAT (Fig. 4b,c). Similar to wild-type P-CE offspring, P-CE offspring from the Ucp1-DTR-GFP line exhibited slightly higher VO_2 and VCO_2 at RT and a significant induction of both parameters after CE at time point I (TP I) (Fig. 4d

and Supplementary Fig. 4a, TP I). When mice were treated with DTA (TP II–IV), we observed a reduction in VO_2 and VCO_2 exclusively in the P-CE offspring (Fig. 4d and Supplementary Fig. 4a, TP II–IV), which, after three consecutive injections of DTA, led to the abrogation of the difference in VO_2 and VCO_2 levels. The RER was not altered between the two groups at any time point (Supplementary Fig. 4b).

To avoid a shivering response in mice that received DTA injections, we analyzed respiration in mice in response to CL injections. We observed higher VO_2 and VCO_2 in P-CE versus Ctrl offspring of Ucp1-DTR-GFP mice after CL treatment (Fig. 4e and Supplementary Fig. 4c, TP I). Because the CL injections caused only a transient increase in respiration, we treated the mice with three subsequent injections of CL and DTA (Fig. 4e and Supplementary Fig. 4c, TP II–IV). After two injections with DTA the difference between P-CE and Ctrl offspring on both VO_2 and VCO_2 was lost, suggesting that brown and brite adipocytes might, in part, be responsible for the observed higher respiration in P-CE offspring. Similarly, we observed a lower RER in P-CE offspring after CL injections, which was lost after DTA injections (Supplementary Fig. 4d). These findings were supported by the observation that 24 h after the third CL + DTA injection, we did not observe any difference in respiration between both groups (Fig. 4f and Supplementary Fig. 4e,f). To analyze whether the observed effects would also translate into an induction of thermogenesis, we quantified surface temperature after an injection of CL, with or without DTA-mediated ablation of brown adipocytes. In accordance with previous data (Fig. 4e), surface temperature was higher in P-CE versus Ctrl offspring after the CL injection (Fig. 4g), and the effect was lost when brown adipocytes were ablated (Fig. 4h). Lastly, we could show that DTA injection did not induce overt inflammation in mice (Supplementary Fig. 4g). Taken together, our data demonstrated that the effect of P-CE on respiration and thermogenesis was, at least in part, mediated through the activation of brown adipocytes.

Cold exposure of paternal mice protects from diet-induced obesity and insulin resistance. Because BAT has been implicated in energy expenditure, we aimed to assess whether body weight and metabolism would be different under challenged conditions. Therefore, we fed P-CE and Ctrl offspring a high-fat diet (HFD), in which 60% of the calories were derived from fat, for 10 weeks. Even though P-CE offspring consumed significantly more food than Ctrl offspring (Fig. 5a), we found that P-CE offspring showed slightly lower body weight gain and reduced fat mass than Ctrl offspring (Fig. 5b,c). Furthermore, we found that P-CE offspring had markedly better insulin sensitivity than Ctrl offspring (Fig. 5d), even though fasting blood glucose levels were similar in both groups of mice. The latter might be due to the lower levels of circulating insulin in P-CE offspring (Fig. 5e). We found significantly lower levels of circulating TAGs in P-CE versus Ctrl offspring (Fig. 5f), whereas there was no difference in cholesterol levels (Fig. 5g).

Of note, we observed a significantly higher metabolic rate indicated by higher VO_2 and VCO_2 levels at RT conditions in P-CE versus Ctrl offspring (Fig. 5h and Supplementary Fig. 5a), whereas we did not observe any changes in substrate utilization, as indicated by an unchanged RER (Supplementary Fig. 5b). This higher oxygen consumption rate (OCR) was paralleled by significantly higher body surface temperature (Supplementary Fig. 5c) and UCP1 expression in iBAT (Supplementary Fig. 5d). Furthermore, we could show that hepatic lipid accumulation was reduced in P-CE versus Ctrl offspring (Fig. 5i,j), which might explain the altered insulin sensitivity. Notably, circulating levels of FGF21, a hormone which has been suggested to be secreted from activated BAT[26] and is known to affect glucose and lipid homeostasis, was higher in P-CE offspring kept on a HFD (Fig. 5k). Taken together, our data demonstrate that under RT conditions, which give mild cold stress, P-CE offspring are partially protected from diet induced obesity and maintain an improved metabolic profile.

Gene expression and DNA methylation analysis of P-CE offspring suggests changes in brown adipocyte formation and neurogenesis. We then asked whether transcriptional changes in iBAT could explain the observed phenotype. Therefore, we performed RNA sequencing (RNA-seq) analysis of iBAT from P-CE and Ctrl offspring at RT and after CE for 3 d. Unbiased hierarchical clustering, including that for all of the genes expressed in at least one sample group, revealed distinct transcriptional profiles for the different conditions (Supplementary Fig. 6a). A principal component analysis (PCA) similarly showed distinct clusters of each of the four sample groups (Fig. 6a). Principal component 1 (PC1) seemed to capture the differences imposed by acute CE. Several genes related to BAT activity, such as glycerol kinase (*Gyk*) or *Ucp1*, were major contributors of negative PC1 loadings, whereas muscle-specific genes contributed to positive PC1 loadings. Notably, samples from P-CE offspring after CE had an even stronger negative PC1 loading than the Ctrl samples, indicating a hyperactivated BAT condition in P-CE offspring.

A pairwise differential gene expression analysis that compared Ctrl offspring at RT versus after CE (Ctrl-RT versus Ctrl-CE) and that considered at least a twofold mean expression difference to be significant (Supplementary Table 1) identified many genes related to BAT activity (Supplementary Fig. 6b,c). Consistent with the PCA, we also found a number of genes that were upregulated in the CE samples from P-CE offspring versus Ctrl offspring to be related to BAT activity (Fig. 6b), as well as an enrichment of gene ontology (GO) terms related to high metabolic activity in all significantly regulated genes (Fig. 6c). Of note, *Adrb3* and *Ucp1* were also significantly differentially expressed; however, the regulation was < 2-fold between cold-exposed P-CE and Ctrl offspring; therefore, these genes were not included in the GO analysis.

Because phenotypic and transcriptional changes of P-CE offspring are mediated through the sperm via the paternal lineage, we performed whole-genome bisulphite sequencing (WGBS) of sperm (sixfold average genomic coverage in each sample) to identify possible DNA methylation alterations that could potentially mediate the intergenerational transmission of the observed phenotype (Fig. 6d). We observed a small but significantly greater degree of global 5′-cytosine-phosphate-guanine-3′ (CpG) DNA methylation in the P-CE samples (89.5% versus 87.5%; P value < 0.002; Fig. 6e), which indicated an effect of CE on the sperm methylome.

To analyze whether methylation levels were altered in genomic regions that might affect gene expression in the offspring, we first performed hierarchical clustering and PCA of the methylation status of all promoter regions (Fig. 6f and Supplementary Fig. 6d). We observed a clear separation between P-CE and Ctrl sperm samples and a distinguishable clustering of the two groups in the PCA. In contrast to global CpG methylation, we found a small, but significant, reduction in the average methylation levels of CpG islands (CGI) in the P-CE samples (Supplementary Fig. 6e). Hierarchical clustering and PCA of all non-CGI promoters showed comparable levels of separation on PC1 but less clear clustering, suggesting that the differences in CGI methylation were relevant contributors to the observed differences in promoter methylation.

These analyses indicated that the CE-induced methylation changes in sperm were reproducible and contributed to the observed phenotypic differences in the offspring. It is important to note that sperm is a haploid cell type, and as such, single CpG sites can only be either methylated or unmethylated. To address this issue, we decided to subdivide the genome in probes of 50 adjacent CpGs and analyze methylation changes over these probes. An unbiased analysis of the P-CE and Ctrl sperm methylome datasets identified 2,431 DMRs with an overlapping or downstream (maximum 2 kb)

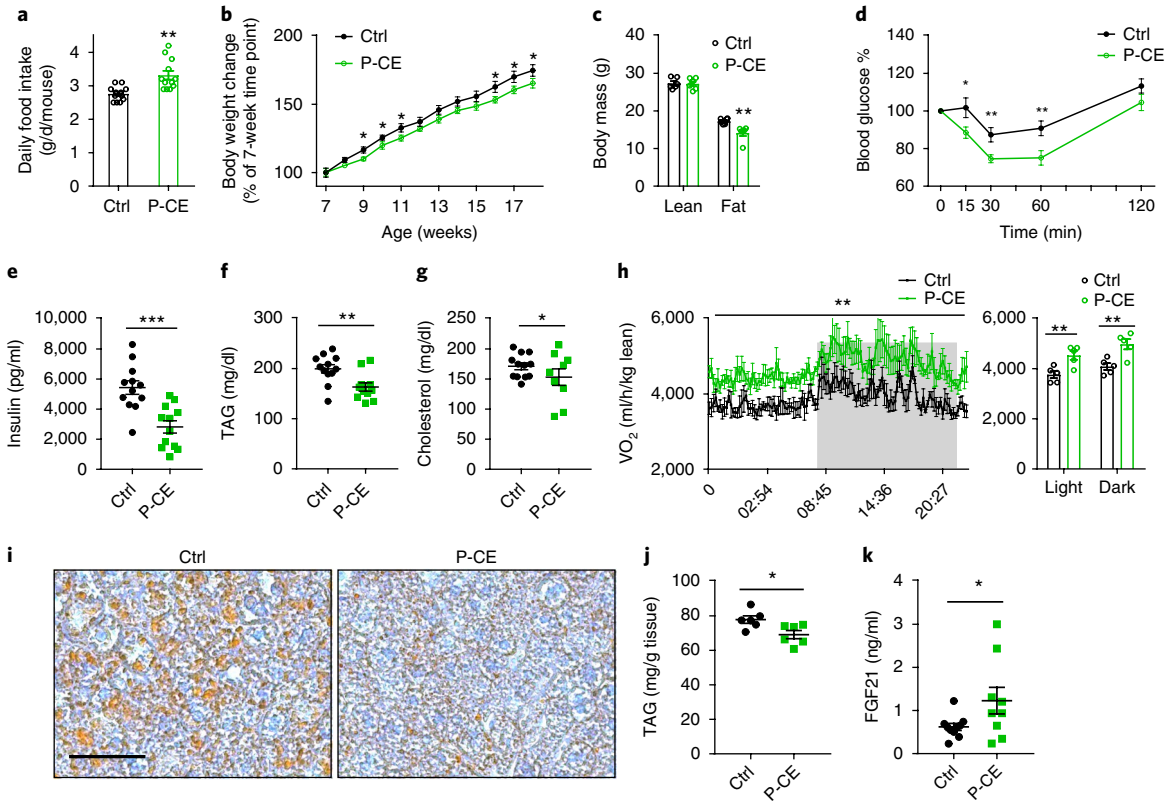

Fig. 5 | Paternal cold exposure protects offspring from high-fat-diet-induced obesity. a–c, Daily food intake ($n=12$) (**a**), body weight gain ($n=11$) (**b**) and body composition ($n=6$) (**c**) of Ctrl and P-CE offspring mice that were fed a HFD, at RT for the indicated amounts of time. **d**, Insulin tolerance test of Ctrl or P-CE offspring that were fed a HFD for 7 weeks at RT, with 6 h of fasting ($n=12$). Shown is one representative of three independent experiments. **e–g**, Circulating insulin ($n=12$) (**e**), TAG ($n=11$) (**f**) and cholesterol ($n=9$) (**g**) levels of Ctrl or P-CE offspring that were fed a HFD for 11 weeks at RT. **h**, Time-resolved oxygen consumption time course and analysis of Ctrl or P-CE offspring that were fed a HFD for 11 weeks at RT. Graph depicts calculated mean as indicated ($n=5$). $P=0.001$. **i**, Representative Oil red O staining on liver sections of Ctrl or P-CE offspring that were fed a HFD for 11 weeks at RT ($n=6$ litters). Scale bar, 200 µm. **j**, TAG content in the liver of the indicated mice ($n=6$). **k**, Circulating FGF21 levels of Ctrl or P-CE offspring on a HFD ($n=9$). Throughout, results are mean ± s.e.m.; $n=$ number of litters tested, each dot represents one litter. Statistical significance was calculated by a two-tailed unpaired Student's *t*-test; $^{*}P<0.05$, $^{**}P<0.01$, $^{***}P<0.001$.

gene (Fig. 6g and Supplementary Table 2). GO enrichment analysis of DMRs that were hypomethylated in the P-CE samples showed a relation to many 'neurogenesis' terms (Fig. 6g). A specific analysis of *Adrb3*, which encodes an important regulator of BAT activity, revealed local hypomethylation in the coding region (false discovery rate (FDR) = 0.01). An independent pyrosequencing analysis of individual CpG sites at the *Adrb3* locus in sperm samples confirmed this result (Supplementary Fig. 6f) and showed that the CpGs at the *Adrb3* locus were hypomethylated in the iBAT and ingWAT from adult P-CE mice (Supplementary Fig. 6g,h). Notably, the transcriptomic analysis had shown that *Adrb3* was also significantly more highly expressed in P-CE iBAT than Ctrl iBAT (Figs. 2c and 6b). To test whether this effect was mediated by DNA methylation, we generated an *Adrb3* overexpression plasmid with a CpG-free backbone and in which all (or none, as control) of the CpGs of *Adrb3* had been methylated in vitro. We then transfected the methylated and nonmethylated plasmids into cells that did not express *Adrb3* (Supplementary Fig. 6i) and confirmed the methylation status of the CpG sites in the transfected plasmids (Supplementary Fig. 6j). We found that expression of *Adrb3* from the methylated plasmid was significantly lower than that from the unmethylated plasmid, suggesting that DNA methylation at the *Adrb3* locus influenced *Adrb3* expression.

Next we elucidated whether the differential methylation status in the sperm of the P-CE and Ctrl samples was directly correlated with transcriptional changes in iBAT tissue. Therefore, we analyzed the expression levels of genes that overlapped with DMRs and that were either hypermethylated or hypomethylated in P-CE sperm. Of note, we found that the average expression levels of transcripts that overlapped with hypermethylated sperm P-CE DMRs were significantly increased as compared to the expression levels for all transcripts, whereas inversely, the expression of transcripts that overlapped with hypomethylated DMRs was significantly lower than the expression of all transcripts in iBAT tissue (Fig. 6h). Gene body methylation is a feature of transcribed genes, although the exact functions are not known[27,28], and it is therefore possible that the identified sperm DMRs could contribute to the greater formation of iBAT tissue in P-CE animals and might contribute to the observed intergenerational effect. We also found that a number of transcripts were significantly differentially expressed in the iBAT of cold-exposed P-CE versus Ctrl samples and that they overlapped with hypo- or hypermethylated DMRs in the respective sperm samples, highlighting a potential direct effect of germline methylation levels and iBAT expression levels for selected genes (Fig. 6i). Taken together, our analyses support our findings that the iBAT from P-CE mice is hyperactivated, which is, in part, dependent on enhanced brown adipocyte formation, as reflected by the upregulated brown adipocyte markers and downregulated muscle-specific genes, possibly due to increased neuronal innervation.

P-CE leads to a cell autonomous increase in brown adipocyte formation. To assess whether brown adipocyte formation was

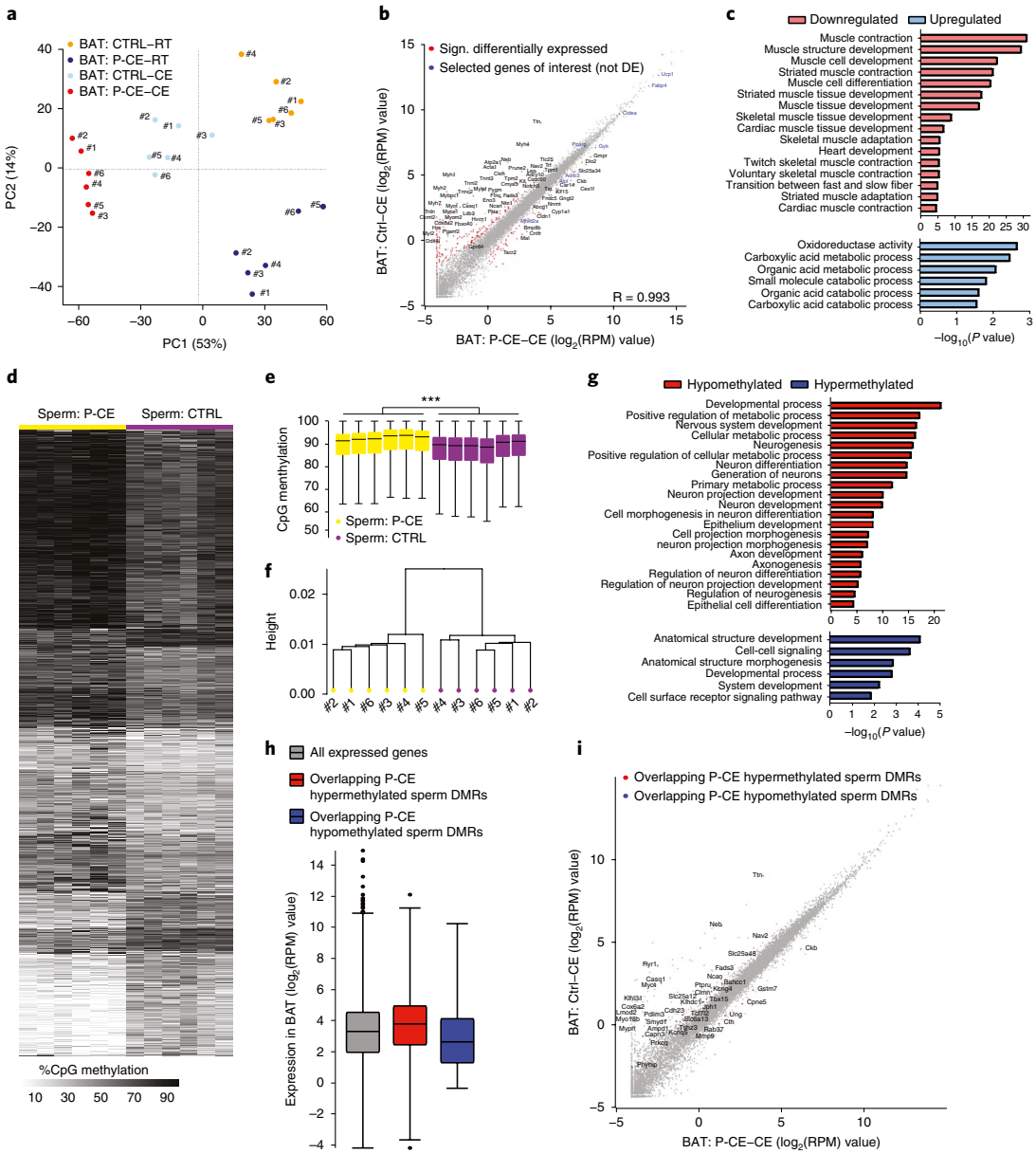

Fig. 6 | Paternal cold exposure affects the transcriptional signature of the brown adipose tissue in the offspring and the epigenetic profile of the sperm. **a**, PCA of RNA-seq data from BAT samples. PC1 and PC2 for each sample were calculated using the SeqMonk PCA pipeline ($n=6$ litters). **b**, Scatter plot of RNA-seq data from BAT samples, comparing P-CE versus Ctrl samples following 3 d of CE. Plotted are the $\log_2$-transformed normalized reads per million (RPM) values. Significant DEGs (overlap between DEseq2 and EdgeR) with at least twofold mean expression differences are highlighted in red. Selected genes of interest that did not fulfill all of the above criteria are labeled in blue and are only shown for comparison with the literature, ($n=6$). **c**, GO terms of upregulated and downregulated genes in iBAT samples from cold-exposed P-CE versus Ctrl offspring ($n=6$ litters). **d**, Heat map showing the methylation levels in DMRs between P-CE and Ctrl sperm samples ($n=6$ mice per group). Clustering of DMRs was performed in SeqMonk. **e**, Box-and-whisker plots showing the CpG methylation levels of individual replicates of sperm samples from P-CE and Ctrl samples. Methylation was quantified over consecutive probes spanning 50 CpGs. Significance was calculated by using the mean CpG methylation levels of P-CE versus Ctrl samples by a two-tailed unpaired Students t-test ($n=6$ mice). $P=0.00052$. **f**, Hierarchical clustering of promoter CpG methylation levels. **g**, GO terms of hyper- and hypo-DMRs in P-CE versus RT sperm ($n=6$ mice). **h**, Expression levels of transcripts in BAT samples that overlap with sperm DMRs that are either hypermethylated or hypomethylated in the paternal CE versus control samples. Shown are the $\log_2$(RPM) values of gene expression levels in BAT ($n=6$ mice). Significance was calculated from the average gene expression levels of each group by a two-tailed unpaired Student's t-test. Number of all expressed genes is 11,334; number of genes that overlapped with P-CE hypermethylated sperm DMRs is 1,049; number of genes that overlapped with P-CE hypomethylated sperm DMRs is 365; "All expressed genes" versus "Genes overlapping P-CE Hypermethylated Sperm DMRs", $P=3.7\times10^{-14}$; "All expressed genes" versus "Genes overlapping P-CE Hypomethylated Sperm DMRs", $P=1.4\times10^{-6}$. Any individual points that fall outside this range are shown as filled circles. Each circle represents a single probe. **i**, Scatter plot of RNA-seq data from BAT samples, comparing P-CE versus Ctrl samples following 3 d of CE. Plotted are the $\log_2$-transformed normalized RPM values. Highlighted are all genes that were significantly differentially expressed (overlap between DEseq2 and EdgeR with at least twofold mean expression differences) in samples between 3-d cold-exposed P-CE and Ctrl mice and that overlapped with identified sperm DMRs. In **e**,**h**, shown are box plots of the CpG methylation percentages of tiling probes spanning 50 CpGs each; the middle line indicates the median of the data; the upper and lower extremities of the box show the 25th and 75th percentiles; and the upper and lower black whiskers show the median ± the interquartile range (25–75%) multiplied by 2. ***$P<0.001$.

indeed altered in P-CE offspring, we isolated the stromal vascular fraction (SVF) from the iBAT of P-CE and Ctrl mice and differentiated these cells into mature brown adipocytes ex vivo. When we analyzed lipid droplet staining, we did not observe any differences between the two groups of cells in either cell numbers or the appearance of multilocular cells (Supplementary Fig. 7a–c). However, we observed a significant increase in the percentage of UCP1$^+$ cells but not in the average intensity of UCP1 staining in UCP1$^+$ cells (Supplementary Fig. 7a,d,e), suggesting that there was an increased propensity to form brown adipocytes. We observed a significant induction of UCP1 protein and *Ucp1* mRNA in P-CE-offspring-derived cells (Supplementary Fig. 7f,g). Similar to our observations for UCP1, we observed a higher mRNA expression of *Adrb3* and cell-death-inducing DFFA-like effector a (*Cidea*) in P-CE-offspring-derived cells, whereas peroxisome proliferator-activated receptor gamma (*Pparg*) levels were the same (Supplementary Fig. 7h–j).

To analyze whether these changes would translate into altered functionality, we quantified the OCR of these ex-vivo-differentiated cells. Although we did not observe any changes in basal OCR, we could show that cells from P-CE offspring had a significantly higher OCR than cells from Ctrl offspring under CL-stimulated conditions (Supplementary Fig. 7k).

To confirm these findings, we quantified ADRB3 protein levels in P-CE and Ctrl offspring. In accordance with the mRNA data, we observed higher ADRB3 expression in P-CE offspring than in Ctrl offspring at the RT, CE and TN conditions (Supplementary Fig. 7l). Given the widespread expression of *Adrb3*, we also analyzed its expression in ingWAT, epididymal adipose tissue (epiWAT) and heart (Supplementary Fig. 7m) and observed an upregulation of *Adrb3* mRNA expression in ingWAT and epiWAT, but not in heart. To analyze whether this regulation could be connected to the DMR pattern that suggested an alteration in neurogenesis-related genes, we analyzed tyrosine hydroxylase (TH) expression in iBAT from P-CE and Ctrl offspring and found that it was increased at both RT and after 2 d of CE in the P-CE offspring (Supplementary Fig. 8a); we also observed higher TH-immunostaining in neuronal axons within the iBAT of the P-CE offspring (Supplementary Fig. 8b,c). We checked vascularization by staining with isolectin B4 (IB4) and found that the iBAT from P-CE offspring was enriched with blood vessels (Supplementary Fig. 8d,e). These data suggested that the iBAT from P-CE offspring was more densely innervated and vascularized, which could explain the hyperactive state.

To test this hypothesis at a functional level, we performed microdialysis of the iBAT from P-CE and Ctrl offspring. We observed an increased release of norepinephrine in P-CE offspring in response to a cold stimulus (Supplementary Fig. 8f). Furthermore, when we blocked adrenergic signaling in vivo, either with the selective ADRB3 antagonist L748,337 or the nonspecific β-blocker propranolol before CE, we observed that similar to BAT ablation, pretreatment with L748,337 or propranolol blocked the effect of P-CE on OCR (Supplementary Fig. 8g,h). Taken together, these data demonstrated that P-CE led to higher neuronal innervation and norepinephrine release in the iBAT of P-CE-derived offspring, whereas blocking β-adrenergic receptor signaling in general, or ADRB3 in particular, abrogated the effect of P-CE.

Discussion

Paternal adaptation to environmental cues have been linked to various physiological changes in the offspring using different animal model systems[22,29]. Our data indicate that CE can be a determinant of the offspring's physiology. This finding is consistent with a recent study suggesting that seasonality can affect systemic metabolism[23,30–33] and that temperature-sensing might influence physiological adaptation. A possible implication for clinical weight-loss studies could be randomization stratified by birth season; however, such a mechanism would have to be investigated in a prospective trial. Furthermore, despite the large number of individuals studied in our cohort and the low *P* value, our results still need to be interpreted with caution. First, the retrospective nature of the study and the inclusion of individuals undergoing FDG-PET/CT introduces numerous biases. Because BAT was not specifically stimulated, an unknown proportion of 'BAT$^-$'-labeled individuals may still have functional but inactive BAT. Second, the location of birth and conception are unknown, which is problematic as there were at least two major immigration waves to Switzerland from southern parts of Europe in the past century[34]. Third, the climate in Switzerland varies substantially and ranges from a mild, Mediterranean-like climate to arctic conditions. Moreover, the clothing style of individuals may not always correlate with the absolute outside temperature, but rather with the perceived meteorological season. Lastly, the amount of daylight has been shown to negatively correlate with BAT activation[35], and it is an inseparable confounder in this kind of retrospective cohort study.

On the basis of our data we propose that preconception CE of male mice leads to a higher degree of inducibility of brown fat, which is consistent with previous work demonstrating that seminal plasma can be the carrier for phenotypic alterations[36]. A possible explanation for the lack of transmission via the maternal lineage is the anatomical location of testis, which is directly exposed to changes in temperature[37]. Nevertheless, it remains unclear whether sperm directly senses temperature or whether the effect is due to a signal derived from other cells. Although de novo methylation is initiated at ~E13.5 in mitotically arrested prospermatogonia, and the methylome is completely established before birth, de novo methylation is not initiated until after birth in the female germline. As a result, the sperm methylome is dependent on faithful DNA methylation maintenance, whereas the oocyte methylome is purely reflective of de novo methylation events. Furthermore, it should be noted that CE does generally not have the capacity to promote genetic mutations; therefore, the observed phenomenon is not driven by genetic inheritance but by (environmental) epigenetic inheritance.

The observed relative increase in basal brown fat UCP1 protein expression at RT in P-CE offspring might be due to the fact that 23 °C constitutes a mild cold challenge to mice[38]. The observed reduction in circulating TAGs is consistent with a previous report demonstrating that BAT is a major sink for TAGs[39], whereas the higher NEFA levels during fasting in P-CE versus Ctrl mice could be due to enhanced ADRB3 signaling in WAT.

Multiple studies have implicated that BAT has an important role in metabolism; however, very few studies have quantified the actual contribution of BAT. Because *Ucp1* deletion requires breeding and housing at TN, use of *Ucp1*-knockout mice might influence the physiological response[40]. By using an acute model of DTA-targeted ablation exclusive to brown and active brite adipocytes[25], we were able to show that BAT, at least in part, mediated the observed metabolic changes, even though changes in heart and white fat, or in inflammatory responses, could account for parts of the metabolic alterations.

On the basis of our results, we propose that paternal cold induces a hyperactive state in the BAT of the offspring, which leads to improved adaptation to overnutrition and hypothermia. Various DMRs did overlap with, or were in close proximity to, genes annotated for neurogenesis. Furthermore, the observed denser neuronal innervation, higher vascularization and increased norepinephrine release in iBAT[41] highlighted that multiple genes contributed to this complex phenotype. Together these results suggest the CE affects the sperm methylome, raising the possibility that altered sperm DNA methylation in cold-exposed fathers contributes to the observed phenotype. It is worth noting that this is, to our knowledge, the first example in which adult CE leads to significant alterations in sperm methylation. Although recent studies have shown that 'epivariation', i.e., stochastic individual differences in DNA methylation,

can be the major contributor to the sperm methylome[42], we would like to point out that the significant concordant global methylation changes, as well as the clear separation of promoter methylation profiles in the sperm of P-CE mice versus that in Ctrl animals, suggest a direct effect of CE on the sperm methylome. Nonetheless, whether these modifications are causative or whether other epigenetic modifications that can convey inherited traits[43], such as histone modifications[44] or long noncoding and small RNAs[45], contribute to the observed phenotype remains to be analyzed.

The phenomenon identified here may also have implications for evolutionary biology, as adaptation to environmental temperature changes is critical for any organism. Intergenerational memory of past CEs may have been one mechanism to improve the survival of the offspring during prolonged phases of CE, such as in the ice age 2.6 million years ago. In conclusion, through modulation of genetic and epigenetic variances, environmental changes might influence adipose tissue and metabolism not only in the exposed individual but also in the next generation. Such mechanisms might be exploitable to design therapies and personalized strategies to induce BAT functionality to counteract obesity and comorbidity diseases.

Methods

Methods, including statements of data availability and any associated accession codes and references, are available at https://doi.org/10.1038/s41591-018-0102-y.

Received: 23 November 2017; Accepted: 21 May 2018;
Published online: 09 July 2018

References

1. World Health Organization. Obesity and overweight. Retrieved 22 June, 2018 http://www.who.int/news-room/fact-sheets/detail/obesity-and-overweight (2017).
2. Rosen, E. D. & Spiegelman, B. M. What we talk about when we talk about fat. *Cell* **156**, 20–44 (2014).
3. Tseng, Y. H., Cypess, A. M. & Kahn, C. R. Cellular bioenergetics as a target for obesity therapy. *Nat. Rev. Drug Discov.* **9**, 465–482 (2010).
4. Frontini, A. & Cinti, S. Distribution and development of brown adipocytes in the murine and human adipose organ. *Cell Metab.* **11**, 253–256 (2010).
5. Bartelt, A. & Heeren, J. Adipose tissue browning and metabolic health. *Nat. Rev. Endocrinol.* **10**, 24–36 (2014).
6. Cannon, B. & Nedergaard, J. Brown adipose tissue: function and physiological significance. *Physiol. Rev.* **84**, 277–359 (2004).
7. Rosenwald, M. & Wolfrum, C. The origin and definition of brite versus white and classical brown adipocytes. *Adipocyte* **3**, 4–9 (2014).
8. Hany, T. F. et al. Brown adipose tissue: a factor to consider in symmetrical tracer uptake in the neck and upper chest region. *Eur. J. Nucl. Med. Mol. Imaging* **29**, 1393–1398 (2002).
9. Cypess, A. M. et al. Identification and importance of brown adipose tissue in adult humans. *N. Engl. J. Med.* **360**, 1509–1517 (2009).
10. Saito, M. et al. High incidence of metabolically active brown adipose tissue in healthy adult humans: effects of cold exposure and adiposity. *Diabetes* **58**, 1526–1531 (2009).
11. van Marken Lichtenbelt, W. D. et al. Cold-activated brown adipose tissue in healthy men. *N. Engl. J. Med.* **360**, 1500–1508 (2009).
12. Virtanen, K. A. et al. Functional brown adipose tissue in healthy adults. *N. Engl. J. Med.* **360**, 1518–1525 (2009).
13. Zingaretti, M. C. et al. The presence of UCP1 demonstrates that metabolically active adipose tissue in the neck of adult humans truly represents brown adipose tissue. *FASEB J.* **23**, 3113–3120 (2009).
14. Nedergaard, J., Bengtsson, T. & Cannon, B. Unexpected evidence for active brown adipose tissue in adult humans. *Am. J. Physiol. Endocrinol. Metab.* **293**, E444–E452 (2007).
15. Cypess, A. M. et al. Activation of human brown adipose tissue by a β3-adrenergic receptor agonist. *Cell Metab.* **21**, 33–38 (2015).
16. Yoneshiro, T. et al. Recruited brown adipose tissue as an anti-obesity agent in humans. *J. Clin. Invest.* **123**, 3404–3408 (2013).
17. Carone, B. R. et al. Paternally induced transgenerational environmental reprogramming of metabolic gene expression in mammals. *Cell* **143**, 1084–1096 (2010).
18. Ng, S. F. et al. Chronic high-fat diet in fathers programs beta cell dysfunction in female rat offspring. *Nature* **467**, 963–966 (2010).
19. Jaenisch, R. & Bird, A. Epigenetic regulation of gene expression: how the genome integrates intrinsic and environmental signals. *Nat. Genet.* **33**, 245–254 (2003).
20. Seong, K. H., Li, D., Shimizu, H., Nakamura, R. & Ishii, S. Inheritance of stress-induced, ATF-2-dependent epigenetic change. *Cell* **145**, 1049–1061 (2011).
21. Anderson, L. M. et al. Preconceptional fasting of fathers alters serum glucose in offspring of mice. *Nutrition* **22**, 327–331 (2006).
22. Ng, S. F. et al. Paternal high-fat diet consumption induces common changes in the transcriptomes of retroperitoneal adipose and pancreatic islet tissues in female rat offspring. *FASEB J.* **28**, 1830–1841 (2014).
23. Phillips, D. I. & Young, J. B. Birth weight, climate at birth and the risk of obesity in adult life. *Int. J. Obes. Relat. Metab. Disord.* **24**, 281–287 (2000).
24. Kaufman, M. H. *The Atlas of Mouse Development* (Academic Press, London, 1994).
25. Rosenwald, M., Perdikari, A., Rülicke, T. & Wolfrum, C. Bidirectional interconversion of brite and white adipocytes. *Nat. Cell Biol.* **15**, 659–667 (2013).
26. Hondares, E. et al. Thermogenic activation induces FGF21 expression and release in brown adipose tissue. *J. Biol. Chem.* **286**, 12983–12990 (2011).
27. Jones, P. A. Functions of DNA methylation: islands, start sites, gene bodies and beyond. *Nat. Rev. Genet.* **13**, 484–492 (2012).
28. Yang, X. et al. Gene body methylation can alter gene expression and is a therapeutic target in cancer. *Cancer Cell* **26**, 577–590 (2014).
29. Öst, A. et al. Paternal diet defines offspring chromatin state and intergenerational obesity. *Cell* **159**, 1352–1364 (2014).
30. Lv, J. et al. The associations of month of birth with body mass index, waist circumference and leg length: findings from the China Kadoorie Biobank of 0.5 million adults. *J. Epidemiol.* **25**, 221–230 (2015).
31. Speakman, J. R. & Heidari-Bakavoli, S. Type 2 diabetes, but not obesity, prevalence is positively associated with ambient temperature. *Sci. Rep.* **6**, 30409 (2016).
32. Valdés, S. et al. Ambient temperature and prevalence of obesity in the Spanish population: The Di@bet.es study. *Obes. (Silver Spring)* **22**, 2328–2332 (2014).
33. Yang, H. K. et al. Ambient temperature and prevalence of obesity: a nationwide population-based study in Korea. *PLoS One* **10**, e0141724 (2015).
34. Afonso, A. Immigration and its impacts in Switzerland. *Mediterranean Quarterly* (Duke University Press) **15**(4), 147–166 (2004).
35. Au-Yong, I. T. H., Thorn, N., Ganatra, R., Perkins, A. C. & Symonds, M. E. Brown adipose tissue and seasonal variation in humans. *Diabetes* **58**, 2583–2587 (2009).
36. Adefuye, A. O., Sales, K. J. & Katz, A. A. Seminal plasma induces the expression of IL-1α in normal and neoplastic cervical cells via EP2–EGFR–PI3K–AKT pathway. *J. Mol. Signal.* **9**, 8 (2014).
37. Zhang, Z. et al. Functional analysis of the cooled rat testis. *J. Androl.* **25**, 57–68 (2004).
38. Fischer, A. W., Cannon, B. & Nedergaard, J. Optimal housing temperatures for mice to mimic the thermal environment of humans: an experimental study. *Mol. Metab.* **7**, 161–170 (2018).
39. Bartelt, A. et al. Brown adipose tissue activity controls triglyceride clearance. *Nat. Med.* **17**, 200–205 (2011).
40. Shabalina, I. G. et al. UCP1 in brite (beige) adipose tissue mitochondria is functionally thermogenic. *Cell Rep.* **5**, 1196–1203 (2013).
41. Bronnikov, G., Houstěk, J. & Nedergaard, J. β-adrenergic, cAMP-mediated stimulation of proliferation of brown fat cells in primary culture. Mediation via β1- but not via β3-adrenoceptors. *J. Biol. Chem.* **267**, 2006–2013 (1992).
42. Shea, J. M. et al. Genetic and epigenetic variation, but not diet, shape the sperm methylome. *Dev. Cell* **35**, 750–758 (2015).
43. Rando, O. J. Intergenerational transfer of epigenetic information in sperm. *Cold Spring Harb. Perspect. Med.* **6**, a022988 (2016).
44. Greer, E. L. & Shi, Y. Histone methylation: a dynamic mark in health, disease and inheritance. *Nat. Rev. Genet.* **13**, 343–357 (2012).
45. Daxinger, L. & Whitelaw, E. Understanding transgenerational epigenetic inheritance via the gametes in mammals. *Nat. Rev. Genet.* **13**, 153–162 (2012).

Acknowledgements

We are grateful to M. Stoffel, J. Krützfeldt and members of the Wolfrum lab for helpful discussions, K. Tabbada for assistance with WGBS high-throughput sequencing, and F. Krueger and S. Andrews for help with bioinformatics analysis. We thank K. De Bock and F. Zheng for the IB4 antibody and K. A. Rollins for editing the manuscript. Data produced and analyzed in this paper were generated in collaboration with the Genetic Diversity Center (GDC) and Functional Genomics Center Zurich (FGCZ). The work was supported by the Swiss National Science Foundation (SNSF; C.W. and F.v.M.).

Author contributions

W.S. and C.W. designed the study; W.S. and H.D. performed all of the experimental work, except that described below; P.P. performed the IVF; S.M. helped with the Seahorse experiments; D.H.D. characterized the Ucp1-DTR-GFP mice; C.W., V.E., M.B. and D.H.D. contributed to the tracing of radiolabeled glucose; E.K. did paraffin sectioning; G.G. quantified lipid droplet sizes; A.P. helped with FACS; V.E. performed automated image analysis; L.G.S. helped with indirect calorimetry analysis; G.S. helped in the

analysis of maternal behavior; D.P.-R. and W.S. did the microdialysis studies; A.S.B., I.A.B., S.B. and C.Z. performed the retrospective analysis of BAT in humans; L.O. contributed to RNA-seq data analysis; F.v.M. and W.R. did DNA methylation sequencing and bioinformatic analysis; W.S. and C.W. wrote the manuscript; and F.v.M., A.S.B., I.A.B., D.H.D., S.M., M.B. and L.B. helped with the editing of the manuscript.

Competing interests

The authors declare no competing interests.

Additional information

Supplementary information is available for this paper at https://doi.org/10.1038/s41591-018-0102-y.

Reprints and permissions information is available at www.nature.com/reprints.

Correspondence and requests for materials should be addressed to C.W.

Publisher's note: Springer Nature remains neutral with regard to jurisdictional claims in published maps and institutional affiliations.

Methods

Materials. Details of the reagents used in this study are listed in Life Sciences Reporting Summary.

Human study. 13,502 FDG-PET/CT scans of 8,440 individuals that were examined during November to February in the years 2007–2015 were reviewed for the presence of active BAT by physicians[46]. Uptake in the supraclavicular and cervical area was considered to be grade 1, that in the paravertebral and mediastinal areas were considered to be grade 2 and that in the infradiaphragmal area was considered to be grade 3. Readers were blinded to the hypothesis of this study. The birth dates of the individuals were extracted from the 'digital imaging and communications in medicine' (DICOM) metadata of the images. Density plots of the birthdays were created with ggplot2 2.1.0 in R 3.3.1. (R Foundation for Statistical Computing, Vienna, Austria). The distributions of individuals were examined with a generalized linear model (Poisson error distribution and link function) to estimate the likelihood of being conceived in the cold period of the year. The BAT-negative control cohort was matched for sex and age with the nearest-neighbor algorithm[47]. The mean temperature of northern Switzerland was acquired from the Federal Office of Meteorology and Climatology MeteoSwiss in a monthly resolution. The study was approved by the Cantonal Ethics Committee Zürich.

Mice. Wild-type C57BL/6N mice were obtained from Charles River Laboratories. Ucp1-DTR-GFP mice were generated as described previously[25]. Unless indicated otherwise, all experiments were performed with adult male mice kept on an inverted 12-h:12-h dark:light cycle, fed ad libitum with a chow diet or a 60% HFD. For cold stimulation, animals were housed in long type II cages at 8 °C. All animal studies were approved by the Veterinäramt Zürich.

Culture of primary adipocytes and HEK 293 cells. For cellular separation, dissected adipose tissues were minced with a scalpel blade and incubated in 2.0 ml per mg wet tissue 0.2% collagenase type II in collagenase buffer (25 mM $KHCO_3$, 12 mM KH_2PO_4, 1.2 mM $MgSO_4$, 4.8 mM KCl, 120 NaCl, 1.2 mM $CaCl_2$, 5 mM glucose, 2.5% BSA, 1% penicillin–streptomycin, pH 7.4) for 50 min at 37 °C with occasional resuspension. 10 ml centrifugation buffer (70% PBS, 15% FBS, 15% HistoPaque 1119) was added, and samples were centrifuged for 5 min at 200 *g*. The SVF pellet from the initial centrifugation was resuspended in 2 ml erythrocyte lysis buffer (154 mM NH_4Cl, 10 mM $KHCO_3$, 0.1 mM EDTA, pH 7.4) and incubated for 4 min on ice. Samples were filtered through 40-µm cell strainers and then centrifuged for 5 min at 200 *g*. The supernatant was removed, and the pellets were resuspended in culture medium (10% FBS and 1% P/S in DMEM); SVF cells were plated in a plate that was precoated with collagen I and differentiated as described previously[48]. Cells were re-fed every 48 h with 1 µM rosiglitazone and 0.5 µg/ml insulin. Fully differentiated adipocytes were stimulated with CL-316,243 (10 nM) at day 8 (iBAT).

The human HEK293A cell line (Invitrogen) was grown at 37 °C, 5% CO_2 in Dulbecco's modified Eagle's medium (DMEM) supplemented with 10% FBS and 1% penicillin–streptomycin. All cells in culture were routinely screened for mycoplasma contamination.

In vitro fertilization (IVF). Spermatozoa isolated from cold-treated and control males were used to fertilize oocytes isolated from superovulated C57BL/6 females. The 4-week-old females were superovulated by i.p. administration of 5 IU of equine chorionic gonadotropin (PMSG) and 5 IU of human chorionic gonadotropin (hCG). Males were euthanized, and the dense sperm were isolated from the cauda epididymis and capacitated in 200 µl of Fertiup medium (Cosmo Bio) for 45 min at 37 °C and 5% CO_2. Following sperm capacitation, 2 µl of sperm solution was added to the IVF drop, which consisted of 100 µl HTF medium (Cosmo Bio) overlaid with embryo-tested mineral oil (Sigma). The oviducts were immediately dissected, and the oocyte clutches were released into the IVF drop. The IVF reaction was performed for 4 h at 37 °C and 5% CO_2. Following the IVF procedure, oocytes were washed several times in M16 medium, and the efficiency of fertilization was ascertained by the appearance of the pronuclei and the second polar body. Fertilized oocytes were surgically transferred into pseudo-pregnant CD1 foster females that had previously been mated with genetically vasectomized Prnm1GFP males[49].

Body composition measurement. Body composition was measured with the EchoMRI 130 instrument (Body Composition Analyzer, Echo Medical Systems). Mice were fasted for 4 h before measurement.

Indirect calorimetry. Indirect calorimetry measurements were performed with the Phenomaster (TSE Systems) according to the manufacturer's guidelines and protocols. Mice were single-caged and acclimated to the metabolic cages for 48 h before metabolic recording.

Surface temperature measurement. Surface temperature was recorded with an infrared camera (E60; FLIR; West Malling, Kent, UK) and analyzed with FLIR-Tools-Software (FLIR; West Malling, Kent, UK)[50].

Tracing of radiolabeled glucose. Radiolabeled glucose uptake in tissue was measured as described previously[51]. Mice were fasted for 4 h, then [^{14}C]2-deoxyglucose at 8 mM, 14.8 MBq per kg body weight (MBq/kg) was injected by tail vein. 30 min after injection, blood samples were collected, and mice were euthanized by cervical dislocation. iBAT, epiWAT, ingWAT, liver, skeletal muscle, heart and the brain were dissected, weighed and lysed in 10 volumes of 0.5 M NaOH. Radioactivity was measured by liquid scintillation counting (100 µl of lysate in 3.9 ml of Emulsifier-Safe, Perkin Elmer).

Insulin tolerance test (ITT). Mice were fasted for 4 h (chow diet) or 6 h (HFD). Blood was collected from a small incision in the tip of the tail (time 0) and then at 15, 30, 60 and 120 min after an i.p. injection of insulin at 0.6 and 0.75 U per kg body weight for chow-fed and HFD-fed mice, respectively (Actrapid Penfill, Novo Nordisk). Blood glucose levels were measured with a blood glucometer (Accu-Chek Aviva, Roche).

Behavioral studies. Maternal behavior quantification was carried out as previously reported[52]. 9-week-old virgin female mice were bred with 9-week-old RT or P-CE male mice. All pregnant females were single-caged, and behavior was recorded throughout the period of pregnancy and nursing by cameras. Maternal nursing behavior was quantified from delivery to postnatal day 11, based on the video recordings.

Biochemical analysis of plasma. Mice were fasted for 6 h before euthanization. Blood samples were obtained from cardiac puncture, and plasma was collected after centrifugation for 15 min at 3,000 r.p.m. at 4 °C. Cholesterol and triglycerides were measured by enzymatic tests (Roche Diagnostics). Plasma FGF21 levels were analyzed by using the Mouse/Rat FGF-21 ELISA kit (BioVendor). Plasma insulin levels were measured by the Mouse/Rat insulin kit (Meso Scale Discovery). Plasma samples for measuring fasting and refeeding NEFAs was obtained after 12 h of fasting and 4 h of refeeding, by a commercial NEFAs kit (WAKO).

DNA isolation from sperm and adipose tissue. DNA from sperm and adipose tissue was extracted with the QIAamp DNA Mini Kit (Qiagen). Sperm samples were isolated from the cauda epididymis and resuspended in M2 medium (Sigma) for 45 min at 37 °C. Supernatant containing sperm without tissue debris was collected, pelleted (10,000 *g*), washed with washing buffer (150 mM NaCl, 10 mM EDTA pH 8.0) and centrifuged for 10 min at 4,000 r.p.m. The sperm pellet was resuspended in 300 µl lysis buffer (100 mM Tris-Cl pH 8.0, 10 mM EDTA, 500 mM NaCl, 1% SDS, 2% β-mercaptoethanol).

DNA pyrosequencing. 500 ng DNA (from sperm, adipose tissues or HEK cells) was bisulfite-converted with the EpiTect Bisulfite Kit (Qiagen) according to the manufacturer's protocol. 20 ng of this bisulfite-converted DNA was PCR-amplified with the PyroMark PCR Kit (Qiagen). PCR amplification and sequencing primers (reverse primers were biotinylated) were designed using the Pyromark Assay Design v2.0 software (Qiagen). The quality of the PCR products was checked by gel electrophoresis. Pyrosequencing was applied on a PyroMark Q96 ID using PyroMark Reagents (Qiagen). DNA methylation frequency was quantified with the PyroMark software (Qiagen). Specific CpG sites are illustrated in Supplementary Table 3.

In vitro methylation assay. DNA encoding the sequence of mouse *Adrb3* was ordered from Genscript and cloned into pCpGfree-mcs vector (Invivogen). HEK293 cells, with 80% confluency in 24-well plates, were transfected with 1,000 ng/well of either methylated or unmethylated constructs with PEI (Polysciences), at a 4:1 ratio to DNA. 24 h after transfection, medium was replaced. Transfected cells were harvested for analysis 48 h after transfection.

Tissue harvest. Mice were euthanized singly in a CO_2 atmosphere. Popliteal lymph nodes were removed from inguinal depots for analyses of gene expression and for cellular separations. Blood was collected by cardiac puncture, and serum was obtained by centrifuging coagulated blood at 10,000 *g* for 5 min at 4 °C.

Analysis of adipocyte differentiation. Differentiated adipocytes at day 8 were used for differentiation analysis. Briefly, cells in a 96-well optical plate were fixed with 5% formaldehyde at 4 °C for 10 min, followed by three washes with PBS. Cells were stained with LD540 (100 ng/µl) for lipid droplets[53] and Hoechst no. 33342 (100 ng/µl). For UCP1 staining, lipids were depleted by treatment with 5% acetic acid in ethanol for 10 min at –20 °C, and cells were washed with PBS twice at RT and blocked in 0.05% Triton X-100 and 5% BSA in PBS. Cells were incubated with a UCP1-specific antibody (1:500; Thermo Fisher PA1-24894) overnight, washed thrice in PBS, incubated with Alexa-Fluor-488-conjugated anti-rabbit-IgG (1:500) secondary antibody and DAPI (to stain nuclei), followed by three washing steps. 29 images per well were taken with an automated microscope imaging system (Operetta, Perkin Elmer). Images were analyzed using the Operetta imaging software as described previously[54].

Histology and image analysis. Adipose tissues were excised, fixed in fresh 4% paraformaldehyde (Sigma) in PBS (Gibco; pH 7.4) for 24 h at 4 °C and

then embedded with paraffin. 4-µm-thick paraffin sections were subjected to histological staining[55]. Heat-induced antigen retrieval was applied on rehydrated paraffin sections. After blocking with 5% BSA for 1 h, primary antibody (1:200 anti-UCP1; Thermo Fisher) diluted in 5% BSA was applied to sections overnight at 4 °C. After washing with PBS, a secondary antibody (Signal Stain Boost IHC, Cell Signaling) was applied according to Cell Signaling's manual, the sections were washed three times, and the signals were detected using the DAB method (Cell Signaling). Standard H&E staining was performed on rehydrated fat-paraffin sections. Slides were dehydrated and covered with coverslip by resin-based mounting. Analysis of lipid droplet sizes was performed using ImageJ. For each treatment, 21–33 pictures were analyzed. Approximately 18,000–58,000 lipid droplet objects per mouse were used for the computation of lipid droplet size. Oil red O staining was applied on liver cyrosections, as previously described[56]. Liver samples were excised, fixed with paraformaldehyde, dehydrated with 30% sucrose and embedded in OCT (Thermo 6502). 10-µm-thick sections were cut and stained with freshly prepared ORO (Sigma O0625) staining solution. All images were acquired by an Axioscope A.1 instrument. Representative images were selected in a blinded fashion.

Fluorescence immunostaining of adipose cryosections. BAT from Ctrl and P-CE mice were excised and fixed in fresh 4% paraformaldehyde (Sigma-Aldrich) in PBS (Gibco) at pH 7.4 for 2 h at 4 °C, washed four times in PBS and cryopreserved for 30 h in 30% sucrose in PBS with stirring at 4 °C. The samples were flash-frozen on dry ice and stored at −80 °C. BAT samples were cut at −25 °C on an HM 500 O microtome (Microm) at 20-µm thickness, mounted on Superfrost plus slides (Medite), thawed at 4 °C, blocked with 10% donkey serum in PBS for 1 h, and treated with a TH-specific antibody (1:200 in PBS) overnight. Sections were washed three times in PBS at RT, stained with Alexa-Fluor-488-conjugated anti-rabbit-IgG secondary antibody and 300 nM DAPI for 1 h. Slides were embedded in ProLong Diamond Antifade Mountant (Thermo Scientific). Fluorescence micrographs were acquired on an SP5 confocal microscope (Leica). Background was adjusted by using samples without primary antibody.

Extracellular respiration. Primary brown preadipocytes were counted and plated at a density of 20,000 cells per well of a Seahorse plate and differentiated to confluence. At day 8 post-differentiation induction, mature brown adipocytes were loaded to an XF_{24} Extracellular Flux Analyzer (Seahorse Bioscience), with one injection of CL-316,243 (10 nM).

RNA extraction, cDNA synthesis and quantitative RT–PCR. Total RNA was extracted from tissues or cells using Trizol reagent (Invitrogen) according to the manufacturer's instructions. Reverse transcription was performed to generate a cDNA library by using the High Capacity cDNA Reverse transcription kit (Applied Biosystems), with 1 µg of RNA. Quantitative PCR was performed on a ViiA7 instrument (Applied Biosystems), and relative mRNA concentrations, normalized to the expression of *Rplp0* (also known as *36B4*), were calculated by the $\Delta\Delta C_t$ method. Primer sequences are listed in Supplementary Table 4.

RNA sequencing (RNA-seq), mapping and analysis. RNA from BAT was quality-checked by a TapeStation instrument (GE). All samples had a RNA integrity number (RIN) > 8. The rRNA was depleted, and purified RNA was used for the preparation of libraries using the TruSeq RNA sample preparation kit (Illumina), and the samples were sequenced on a HiSeq 4000 HT instrument. RNA-seq sequences were trimmed using Trim Galor (v0.4.4, http://www.bioinformatics.babraham.ac.uk/projects/trim_galore/) and mapped to the mouse GRCm38 genome assemblies using hisat2 (v2.1.0). Transcripts were defined using the Ensemble annotations over protein-coding mRNAs. Differential expression analysis of mapped RNA-seq data was performed using DESeq2[57] and EdgeR. Significantly different transcripts were called with significance < 0.05 after Benjamimi and Hochberg correction and minimum mean differential expression of twofold. Further analysis was performed using SeqMonk software (http://www.bioinformatics.babraham.ac.uk/projects/seqmonk/). Quantitation of RPM values was performed by using the SeqMonk RNA-seq pipeline quantitation on merged transcripts counting reads over exons, correcting for DNA contamination, and $\log_2$-transformation assuming an opposing strand-specific library transformed by percentile normalization using 'Add' to the 75.0 percentile. Gene ontology (GO) analysis was performed using the g:profiler software (http://biit.cs.ut.ee/gprofiler/). Expressed genes were defined where at least one of all four groups (CTRL-3CE, CTRL-RT, P-CE-3CE and P-CE-RT) had a $\log_2$(RPM) value > 0. Transcriptional similarities between the different samples were computed on all expressed genes using hierarchical clustering (R hclust package) with Euclidian distances and by applying the Ward distance function and plotted as a dendrogram. PCA was performed using the R prcomp package with default parameters.

Whole-genome bisulfite sequencing (WGBS) mapping and analysis. Genomic sperm DNA was isolated as described and used for WGBS libraries[58]. Briefly, WGBS libraries were prepared by sonicating 500 ng genomic DNA with a Covaris Sonicator into 300- to 400-bp-long fragments, followed by end repair, A-tailing and methylated adaptor (Illumina) ligation using NEB-Next reagents. Libraries were bisulfite treated using the EZ DNA Methylation-Direct Kit (Zymo), followed by library amplification with indexed primers using KAPA HiFi Uracil + HotStart DNA Polymerase (Roche). All amplified libraries were purified with AMPure XP beads (Agencourt) and assessed for quality and quantity by using High-Sensitivity DNA chips (Agilent Bioanalyzer). High-throughput sequencing of all libraries was performed with a 125-bp paired-end protocol on a HiSeq 2000 instrument (Illumina). Raw sequence reads from WGBS libraries were trimmed to remove poor-quality reads and adaptor contamination, using Trim Galore (v0.4.4, http://www.bioinformatics.babraham.ac.uk/projects/trim_galore/). The remaining sequences were mapped using Bismark (v0.18.0)[59] with default parameters to the mouse reference genome GRCm38 in paired-end mode. Reads were deduplicated, and CpG methylation calls were extracted from the deduplicated mapping output using the Bismark methylation extractor (v0.18.0) in paired-end mode. CpG methylation calls were analyzed using R and SeqMonk software (http://www.bioinformatics.babraham.ac.uk/projects/seqmonk/). The genome was divided into consecutive probes that had overlapping 50 CpGs each, and the percentage methylation was calculated with the bisulfite feature methylation pipeline in SeqMonk. Global CpG methylation levels were illustrated by using box whisker plots, and promoter methylation similarities between the samples were assessed by using hierarchical clustering (R hclust with Pearson distances and Ward distance function) and PCA (R prcomp package with default parameters). CGI methylation levels were calculated using the SeqMonk bisulfite feature methylation pipeline and averaged over all CpG islands for illustrations. DMRs were calculated using the SeqMonk binomial filter on probes (50 CpG probes or CGIs) with significance < 0.05 after multiple-testing correction and a minimum difference of 10%. GO analysis was performed using the g:profiler software (http://biit.cs.ut.ee/gprofiler/) with genes that either overlapped with DMRs or were up to 2 kb downstream of the DMR. DMRs were divided into 'hypermethylated' or 'hypomethylated' in the paternal CE versus control samples. The expression levels of transcripts overlapping with DMRs (logistic regression filter; see above) either hypermethylated or hypomethated in the BAT samples from P-CE versus Ctrl mice was computed using the $\log_2$(RPM) gene expression levels in Ctrl BAT samples.

Western blot analysis. Protein samples were isolated from adipose tissue with RIPA buffer (50 mM Tris-HCl pH (7.5), 150 mM NaCl, 1 mM EDTA, 1% Triton X-100, 0.1% SDS and 10% glycerol) supplemented with protease inhibitor cocktail (Roche) and Halt phosphatase inhibitor (Thermo Scientific). Homogenized protein lysates were obtained by rotation at 4 °C for 30 min, followed by centrifugation at 14,000 r.p.m. for 30 min. Protein amounts were quantified using the DC Protein Assay (Bio-Rad). For immunoblotting, protein samples were separated by SDS-PAGE on 12% polyacrylamide gels and transferred onto nitrocellulose membrane. Membranes were probed using the indicated antibodies, and chemiluminescent signals were detected by a LAS 4000 mini Image Quant system (GE Healthcare). Band intensity was quantified using ImageJ. Uncropped full scan blots are shown in Supplementary Figs. 9–11.

In vivo microdialysis from iBAT. For measuring the release of norepinephrine from iBAT, a microdialysis probe was implanted subcutaneously on the back of the mouse 1 h before the start of the experiment (CMA 20 custom-made, 3-mm membrane, cutoff 20,000 kDa; CMA, Sweden). The microdialysis probe was connected to a pump that flushed artificial cerebrospinal fluid (147 mM Na^+, 2.4 mM Ca^{2+}, 4 mM K^+, 155.6 mM Cl^-, pH 6.0) through the probe at a flow rate of 1.5 µl/min. The tube was connected to the mouse via a movable arm to allow free movement. After stabilization, samples were collected at 30-min intervals through a refrigerated fraction sampler (MAB 85, Microbiotech AB, Sweden). After baseline samples at RT were collected, temperature was reduced to 8 °C for a period of 3 h.

Norepinephrine assessment by high-performance liquid chromatography (HPLC). Dialysate samples from BAT were immediately frozen and stored at −80 °C until injection onto the HPLC (Ultimate 3000, Thermo Scientific, USA) system. Norepinephrine levels were detected and analyzed by using an electrochemical detector (ECD-3000RS, Thermo Scientific, USA) with a coulometric cell (6011RS, Thermo Scientific, USA). The samples were injected via a refrigerated autoinjector (Thermo Fisher, CA, USA) equipped with a 100-µl injection loop. Samples were separated on a reversed-phase column (4.6 × 80 mm, 3 µm, Thermo Fisher, USA). We used a HPLC pump (ISO-3100BM, Thermo Fisher, CA, USA) and a mobile phase of ammonium acetate, EDTA, 15% methanol and 5% acetonitrile, adjusted to a pH of 6.0, at a flow rate of 0.3 ml/liter at 32 °C. A chromatography workstation (Chromeleon, Thermo Fisher Scientific, Switzerland) was used for data acquisition and calculation.

Statistical analyses. For in vivo studies, age-matched male mice were used for all experiments. Sample sizes were determined on the basis of previous experiments using similar methodologies. P-CE and Ctrl fathers always were derived from same litters and were handled in the same manner. One or two offspring were used from each litter for all experiments. The number of litters analyzed for all experiments are indicated in the corresponding figure legends. If more than one mouse from one litter was used, then the mice were analyzed as technical replicates. In total, more than 60 litters per group were analyzed for P-CE and Ctrl mice. Mice were randomly assigned to treatment groups. All of the mice were included for statistical

analyses, and the investigators were not blinded to the mice. RNA and DNA methylation sequencing analyses were blinded to experimental conditions. Results are reported as mean ± s.e.m. Two-tailed unpaired Student's *t*-test was applied for comparison. ANOVA was applied on comparisons that involved multiple groups. Statistical differences are indicated as $^{*}P<0.05$, $^{**}P<0.01$ and $^{***}P<0.001$.

Reporting Summary. Further information on experimental design is available in the Nature Research Reporting Summary linked to this article.

Data and software availability. The Gene Expression Omnibus (GEO) accession number for the WGBS next-generation-sequencing data reported in this study is GSE100231. RNA-seq data were uploaded to European Nucleotide Archive (ENA) with accession number PRJEB15274.

References

46. Becker, A. S., Nagel, H. W., Wolfrum, C. & Burger, I. A. Anatomical grading for metabolic activity of brown adipose tissue. *PLoS One* **11**, e0149458 (2016).
47. Ho, D. E., Imai, K., King, G. & Stuart, E. A. Matching as nonparametric preprocessing for reducing model dependence in parametric causal inference. *Polit. Anal.* **15**, 199–236 (2007).
48. Kazak, L. et al. A creatine-driven substrate cycle enhances energy expenditure and thermogenesis in beige fat. *Cell* **163**, 643–655 (2015).
49. Haueter, S. et al. Genetic vasectomy–overexpression of PRM1-EGFP fusion protein in elongating spermatids causes dominant male sterility in mice. *Genesis* **48**, 151–160 (2010).
50. Whittle, A. J. et al. BMP8B increases brown adipose tissue thermogenesis through both central and peripheral actions. *Cell* **149**, 871–885 (2012).
51. Abreu-Vieira, G. et al. Cidea improves the metabolic profile through expansion of adipose tissue. *Nat. Commun.* **6**, 7433 (2015).
52. Pryce, C. R., Bettschen, D., Nanz-Bahr, N. I. & Feldon, J. Comparison of the effects of early handling and early deprivation on conditioned stimulus, context and spatial learning and memory in adult rats. *Behav. Neurosci.* **117**, 883–893 (2003).
53. Spandl, J., White, D. J., Peychl, J. & Thiele, C. Live-cell multicolor imaging of lipid droplets with a new dye, LD540. *Traffic* **10**, 1579–1584 (2009).
54. Meissburger, B. et al. Adipogenesis and insulin sensitivity in obesity are regulated by retinoid-related orphan receptor gamma. *EMBO Mol. Med.* **3**, 637–651 (2011).
55. Sanchez-Gurmaches, J. & Guertin, D. A. Adipocytes arise from multiple lineages that are heterogeneously and dynamically distributed. *Nat. Commun.* **5**, 4099 (2014).
56. Mehlem, A., Hagberg, C. E., Muhl, L., Eriksson, U. & Falkevall, A. Imaging of neutral lipids by oil red O for analyzing the metabolic status in health and disease. *Nat. Protoc.* **8**, 1149–1154 (2013).
57. Love, M. I., Huber, W. & Anders, S. Moderated estimation of fold change and dispersion for RNA-seq data with DESeq2. *Genome Biol.* **15**, 550 (2014).
58. von Meyenn, F. et al. Comparative principles of dna methylation reprogramming during human and mouse in vitro primordial germ-cell specification. *Dev. Cell* **39**, 104–115 (2016).
59. Krueger, F. & Andrews, S. R. Bismark: a flexible aligner and methylation caller for bisulfite-seq applications. *Bioinformatics* **27**, 1571–1572 (2011).

nature research

Corresponding author(s): Prof. Christian Wolfrum

☐ Initial submission ☐ Revised version ☒ Final submission

Life Sciences Reporting Summary

Nature Research wishes to improve the reproducibility of the work that we publish. This form is intended for publication with all accepted life science papers and provides structure for consistency and transparency in reporting. Every life science submission will use this form; some list items might not apply to an individual manuscript, but all fields must be completed for clarity.

For further information on the points included in this form, see Reporting Life Sciences Research. For further information on Nature Research policies, including our data availability policy, see Authors & Referees and the Editorial Policy Checklist.

Experimental design

1. Sample size

Describe how sample size was determined.

For mouse work, sample size was determined based on similar studies in our lab and reported in the literature, which are commonly employed in the field. Each experiment was performed multiple times as indicated in the Figure legends. Samples size of the human cohort was dependent on the availability of subjects.

2. Data exclusions

Describe any data exclusions.

No samples were excluded from any analyses.

3. Replication

Describe whether the experimental findings were reliably reproduced.

Unless stated otherwise, all data shown were performed with at least three independent experiments. Each experiment was performed multiple times as indicated in the figure legends.

4. Randomization

Describe how samples/organisms/participants were allocated into experimental groups.

For each study, animals were randomly allocated into experimental groups.

5. Blinding

Describe whether the investigators were blinded to group allocation during data collection and/or analysis.

If not stated otherwise, investigators were blinded to sample groups during experiments and data analysis. Human data analysis was done by technicians unaware of the study goal.

Note: all studies involving animals and/or human research participants must disclose whether blinding and randomization were used.

6. Statistical parameters

For all figures and tables that use statistical methods, confirm that the following items are present in relevant figure legends (or in the Methods section if additional space is needed).

n/a	Confirmed	
☐	☒	The exact sample size (*n*) for each experimental group/condition, given as a discrete number and unit of measurement (animals, litters, cultures, etc.)
☐	☒	A description of how samples were collected, noting whether measurements were taken from distinct samples or whether the same sample was measured repeatedly
☐	☒	A statement indicating how many times each experiment was replicated
☐	☒	The statistical test(s) used and whether they are one- or two-sided (note: only common tests should be described solely by name; more complex techniques should be described in the Methods section)
☐	☒	A description of any assumptions or corrections, such as an adjustment for multiple comparisons
☐	☒	The test results (e.g. *P* values) given as exact values whenever possible and with confidence intervals noted
☐	☒	A clear description of statistics including central tendency (e.g. median, mean) and variation (e.g. standard deviation, interquartile range)
☐	☒	Clearly defined error bars

See the web collection on statistics for biologists for further resources and guidance.

Software

Policy information about availability of computer code

7. Software

Describe the software used to analyze the data in this study.	Quantification of ICC pictures were done by Operetta imaging software (Perkin Elmer); Quantification of Western Blot was done by ImageJ (NIH); Cell Respiratory analysis was done by XF24 Extracellular Flux Analyzer software (Seahorse Bioscience); Statistical analysis was done by Prism and R. PhenoMaster(mouse 5.6.5), Pyromark Assay Design v2.0, hisat2 v2.1.0, Trim Galore v0.4.4, Bismark v0.18.0.

For manuscripts utilizing custom algorithms or software that are central to the paper but not yet described in the published literature, software must be made available to editors and reviewers upon request. We strongly encourage code deposition in a community repository (e.g. GitHub). *Nature Methods* guidance for providing algorithms and software for publication provides further information on this topic.

Materials and reagents

Policy information about availability of materials

8. Materials availability

Indicate whether there are restrictions on availability of unique materials or if these materials are only available for distribution by a for-profit company.	There are restrictions on the availability of these materials: High Capacity cDNA Reverse transcription kit: Applied Biosystems 4368814 Cholesterol kit: Roche Diagnostics 12016630 Triglycerides kit: Roche Diagnostics 12016648 Mouse/Rat FGF-21 ELISA kit: BioVendor RD291108200R Mouse/Rat insulin kit: Meso Scale Discovery K152BZC NEFAs kit: WAKO WA2 434-91795 cAMP ELISA: ENZO life sciences ADI-900-066 QIAamp DNA Mini Kit: Qiagen 51304 EpiTect Bisulfite Kit: Qiagen 59104 TruSeq kit: Illumina RS-122-2301 DC Protein Assay: Bio-Rad 5000111 AllPrep DNA/RNA micro kit: Qiagen 80284 QuantiTect whole transcriptome kit: Qiagen 207045 3-Isobutyl-1-methylxanthine: Sigma I5879 Dexamethasone: Sigma D4902 Indomethacin: Sigma I7378 Insulin: Sigma I9278 Rosiglitazone: Sigma R2408 Triiodo-L-Thyronine (T3): Sigma T2877 CL-316,243: Sigma C5976 14C-2-deoxyglucose: Perkin Elmer NEC720A050UC Trizol reagent: Invitrogen 15596026 Oil Red O: Sigma O0625 Collagenase type II (clostridium histolyticum): Sigma C6885 Collagen Type I: Sigma C3867 FERTIUP® Preincubation Medium: Cosmo Bio KYD-002-05-EX HTF Medium: Cosmo Bio CSR-R-B071 M16 Medium: Sigma M7292 Penicillin-Streptomycin: Thermo 15070063 DMEM, high glucose: Thermo 41965062 ProLong® Diamond Antifade Mountant: Thermo P36961 Polyethylenimine, Linear (MW 25,000): Polysciences 23966-2 Histopaque 1119: Sigma 11191 Microdialysis probe: CMA Microdialysis , CMA8010464

9. Antibodies

Describe the antibodies used and how they were validated for use in the system under study (i.e. assay and species).

UCP1: ThermoFisher PA1-24894; 1:500(IF), 1:200(IHC);1:1000(WB)
HSP90: Cell Signaling 4877; 1:1000
Glut4 Antibody (C-20); Santa Cruz SC-1608 ; 1:1000
Monoclonal Anti-γ-Tubulin antibody produced in mouse: Sigma-Aldrich; T6557; 1:2000
beta actin mouse monoclonal antibody: Santa Curzsc-47778; 1:500
Anti-beta 3 Adrenergic Receptor antibody: Abcam, AB94506, 1:1000
Tyrosine Hydroxylase: Sigma-Aldrich; AB152 ; 1:200
IB4 Alexa flour 568: ThermoFisher; I21411; 1:1000
Anti-rabbit IgG, HRP-linked Antibody: Cell Signaling, #7074V, 1:4000
Rabbit anti-Goat HRP: Sigm-Aldrich, A5420, 1:4000
Goat Anti-Mouse IgG, H&L Chain Specific Peroxidase Conjugate: Milipore AG; 401253; 1:4000
Alexa Fluor 488 donkey anti-rabbit IgG: Invitrogen; 1:500

10. Eukaryotic cell lines

a. State the source of each eukaryotic cell line used.

Primary cells were used in all experiments used. Detail information regarding primary adipocyte culture is described in Methods - Primary adipocyte culture section. HEK 293A cell line were bought from Invitrogen; #R70507.

b. Describe the method of cell line authentication used.

HEK 293A cell line was authenticated by the vendor. The cell lines were purchased from commercial vendors listed above.

c. Report whether the cell lines were tested for mycoplasma contamination.

All cell cultures were negative for mycoplasma contamination.

d. If any of the cell lines used are listed in the database of commonly misidentified cell lines maintained by ICLAC, provide a scientific rationale for their use.

No commonly misidentified cell lines were used.

Animals and human research participants

Policy information about studies involving animals; when reporting animal research, follow the ARRIVE guidelines

11. Description of research animals

Provide details on animals and/or animal-derived materials used in the study.

Details are stated in Methods - Mice section. Both sexes of C57BL/6 mice (Mus musculus) were obtained from Charles River Laboratory. All animal studies were approved by the Veterinäramt Zürich. All mice were housed in standard conditions with a 12 h light/dark cycle and access to food and water ad libitum. Both sexes of Ucp1-DTR-GFP mice(which created in our lab) were used in this study. The age of mice were described in methods.

Policy information about studies involving human research participants

12. Description of human research participants

Describe the covariate-relevant population characteristics of the human research participants.

FDG-PET scans of 8440 individuals are from University Hospital Zurich (2007 -2015). Details are stated in Methods - Human Study section.